REVISION 1

Germanium distribution in Mississippi Valley-Type systems from sulfide deposition to oxidative weathering: A perspective from Fule Pb-Zn(-Ge) deposit, South China

CHEN WEI[1,2 †], MAX FRENZEL[2], LIN YE[1 *], ZHILONG HUANG[1], AND LEONID DANYUSHEVSKY[3]

[1] State Key Laboratory of Ore Deposit Geochemistry, Institute of Geochemistry, Chinese Academy of Sciences, Guiyang 550081, China

[2] Helmholtz-Zentrum Dresden-Rossendorf, Helmholtz Institute Freiberg for Resource Technology, Freiberg 09599, Germany

[3] Centre for Ore Deposit and Earth Sciences, University of Tasmania, TAS 7001, Australia

[†]Current address: Helmholtz-Zentrum Dresden-Rossendorf, Helmholtz Institute Freiberg for Resource Technology, Freiberg 09599, Germany

* Corresponding author mail: yelin@vip.gyig.ac.cn (L, Ye)

ABSTRACT

Germanium (Ge) is a critical raw material for emerging high-tech and green industries, resulting in considerable recent interest to understand its distribution and geochemical behavior in ore deposits. In this contribution, the distribution of Ge and related trace elements in the Fule Pb-Zn(-Ge) deposit, South China is investigated to reveal the distribution of Ge in the hydrothermal ores and during sulfide weathering, using multiple microanalytical techniques including scanning electron microscopy, electron probe microanalysis and laser ablation-inductively coupled plasma mass spectrometry (LA-ICPMS). In the Fule MVT deposit, sphalerite (ZnS) is the most significant Ge-carrier relative to other sulfides, though the five recognized textural types of sphalerite display progressive depletion in Ge from the first sphalerite generation to the late one. In the early stage, sphalerite with fine-grained chalcopyrite inclusions have the highest Ge concentrations, probably accounting for a significant proportion of the total Ge. We interpret that high Ge concentrations in the early sphalerite may be attributable to high Cu activity in the mineralizing fluids. During oxidative weathering, Ge was redistributed from its original host, sphalerite, to the weathering product willemite (Zn_2SiO_4) rather than smithsonite ($ZnCO_3$), with high levels of Ge (up to 448 μg/g) present in the willemite. The formation of abundant willemite largely prevents the dispersion of Ge during weathering. In principle, willemite-hosted Ge should be fully recoverable, and the Zn-silicate ores may therefore be a potential target to meet future demand. This study provides new information on how Ge behaves from sulfide- to weathering-stage in MVT systems, which directly impact Ge mobility and deportment changes and the development of metallurgical strategies for Ge recovery.

Keywords: Germanium; sulfides; LA-ICPMS, mineral weathering; element mobility

INTRODUCTION

Germanium (Ge) is used in a wide variety of modern high-tech applications (e.g., electronics, infrared instruments, solar panels, fiber optics, etc.) and is widely regarded as a strategic or critical raw material (European Commission 2023; US Geological Survey 2023; Li et al. 2023 and references therein). The growing use of Ge in the electric and optoelectronic devices provides a strong motivation to better understand Ge geochemistry and specifically the factors controlling its behavior in nature. Germanium is largely incorporated into silicate minerals by direct substitution for Si^{4+} despite it occurs in relatively low concentrations (e.g., Bernstein 1985; Höll et al. 2007). In certain environments, Ge exhibits chalcophile, siderophile and organophile behaviors, and is thus preferentially enriched in some types of hydrothermal base-metal deposits, in iron-nickel meteorites and in lignite coal. Currently, Ge is commercially extracted from certain Ge-rich coal and from Zn-/Cu-concentrates, in which Ge is hosted in commonly sulfides, notably sphalerite and sometimes chalcopyrite (Reiser et al. 2011; Frenzel et al. 2017; Belissont et al. 2019), and to a far lesser extent, in enargite and bornite (Cook et al. 2011). Trace element data, including Ge concentrations, have been published on sphalerite, chalcopyrite, pyrite, galena and bornite (Cook et al. 2009, 2011; Ye et al. 2011; Belissont et al. 2014, 2019; Hu et al. 2019; Frenzel et al. 2022, Li et al. 2023 and references therein). However, data on the Ge distribution between various minerals in low-temperature (low-*T*) hydrothermal systems remains relatively sparse (e.g., Hu et al. 2019).

Germanium and other elements, such as Mn, Fe, Co, Ga, In, and Cd, can be incorporated into sphalerite at concentration levels tenths μg/g to wt.% (Cook et al. 2009; Ye et al. 2011; Murakami and Ishihara 2013; Belissont et al. 2014; Wei et al. 2019; Cugerone et al. 2021; Torró et al. 2023 and reference therein). The relative concentrations of these elements can be an indicator for the origin of ore deposits (Ye et al. 2011; Belissont et al. 2014; Frenzel et al. 2016; Wei et al. 2018; Li et al. 2020a)

and the evolution of the mineralizing fluids in different hydrothermal systems (Pfaff et al. 2011; Gagnevin et al. 2012; Wei et al. 2021). Specifically, formation temperature appears to control the occurrence of some elements in sphalerite (Möller 1987; Frenzel et al. 2016). Trace elements such as Mn, Fe, In, and potentially Sn are more concentrated in sphalerite formed in high-*T* (magmatic-)hydrothermal fluids while Ga, Ge, Sb, Tl, and As tend to be enriched in sphalerite formed at low-temperature conditions (e.g., Wei et al. 2018; Frenzel et al. 2022). Upon metamorphic recrystallization, several elements (such as Ge, Pb, Bi, and to some degree Cu and Ag) can be released from sphalerite to form independent minerals, while others are readily re-incorporated into the crystal lattice (Lockington et al. 2014; Cugerone et al. 2018). In contrast, the fate of Ge upon supergene weathering has not received sufficient attention. Weathered ores have been found to contain large amounts of Ge, with concentrations in some locations exceeding those in the original sulfides (Bernstein 1985; Mondillo et al. 2018a). Germanium is commonly enriched in Zn-silicate and Fe-(oxy)hydroxide minerals during the process of weathering (e.g. Mondillo et al. 2018b; Choulet et al. 2019; White et al. 2022). However, partition and redistribution of Ge among different supergene minerals have not been well documented.

The Fule MVT deposit (lat 25° 22′ N, long 104° 23′ E), located at the Sichuan-Yunnan-Guizhou triangle region, South China (Fig. 1A), is an ideal case study for understanding Ge distribution and mineral hosts in MVT hydrothermal systems affected by supergene processes because (i) this deposit is typical for the Ge-rich Pb-Zn deposits of China, with estimated Ge reserves of >330 ton (Si et al. 2013); (ii) the diverse Zn-bearing mineral assemblages from sulfide deposition to weathering are preserved, including pyrite-sphalerite-tennantite±galena, sphalerite-willemite and smithsonite-willemite assemblages; and (iii) detailed geological and geochemical data are available for entire deposit, with good access to representative samples (e.g., Si et al. 2013; Zhou et al. 2018; Li et al.

2020b). In this contribution, compositional analysis using electron probe microanalysis (EPMA) and laser ablation-inductively coupled plasma mass spectrometry (LA-ICPMS) are conducted, based on systematic mineralogical and petrographic observations of distinct types of sphalerite associated sulfides (galena, pyrite, tennantite), carbonate minerals, and willemite. The main goals of the study are revealing the partitioning behavior of Ge and related elements between sphalerite and associated minerals; and evaluating the mobility and redistribution of Ge during supergene weathering. A better understanding of the distribution and hosts of Ge in low-*T* MVT hydrothermal systems directly impacts Ge mobility and deportment changes, guiding metallurgical strategies for Ge recovery.

GEOLOGY OF THE FULE DEPOSIT

The Fule deposit, located 110 km north-northeast of Luoping city, is a typical example of the Ge-rich Pb-Zn deposits in the Sichuan-Yunnan-Guizhou MVT province, China (Si et al. 2013). The exposed stratigraphy in the Fule mining area includes (Fig. 1B): (i) Late Carboniferous dolomitic bioclastic limestone and coarsely crystalline dolostone of the Maoping Formation; (ii) Early Permian quartz sandstone interlayered with shale and coal seams of the Liangshan Formation (conformably overlies the Maoping Formation); (iii) Middle Permian light to dark dolostone and limestone of the Yangxin Formation (main ore-host unit), containing flint nodules in the uppermost units (conformably overlies the Liangshan Formation); (iv) Late Permian basalts, volcanic breccias and tuffs of the Emeishan Formation (disconformably overlies the Yangxin Formation); (v) Late Permian terrestrial coal-bearing pelitic siltstone and silty mudstone of the Xuanwei Formation (disconformably overlie the Emeishan Formation); (vi) Early Triassic sandstone, shale and argillaceous limestone of the Feixianguan Formation (conformably overlies the Xuanwei Formation); (vii) Early Triassic argillaceous limestone of the Yongning Formation (conformably overlies the Feixianguan Formation); and (viii) Middle Triassic greywacke, mudstone and dolostone of the

Guanling Formation. In addition, Quaternary sediments locally overlie the Permian and Triassic rocks.

The main structures in the Fule mining area include the NE-trending Faben anticline and NNE- and N-trending faults (Fig. 1B). The Faben anticline is a gentle fold structure whose axis trends 30°–40° with an axial plane dipping to NE. Carboniferous rocks are exposed in the core of the anticline, while Permian rocks are exposed on the limb. The north-trending F_{1-4} faults are a series of thrust faults and are considered the product of the Late Triassic Indosinian Orogeny. These faults control the occurrence of the Pb-Zn mineralization in the Fule deposit, while the NNE-trending F_{5-7} normal faults are post-ore structures, deforming the original orebodies (Li et al. 2020b).

The Fule ore district contains two mining areas: Fule and Fusheng (from north to south). Orebodies mainly occur as stratiform or lentiform bodies along bedding planes within the Yangxin Formation. Drilling, trenching, and test shafts have discovered 28 different orebodies, with proven resources of ~10 Mt sulfide ore grading 15–20 wt.% Pb+Zn associated with 4567 ton Cd at 256–8171 g/t and >330 ton Ge at 1.77–239 g/t (Si et al. 2013; Zhou et al. 2018). These orebodies occur over a total area of 3.0 km long (towards NW) and 1.5 km wide (towards NE), and trend SE with a dip of 10°. The largest orebody, the Erdong stratiform orebody, is about 1000 m long, 300–500 m wide, 0.1–20 m thick, and contains 4.5 Mt of sulfide ores with an average ore grade of 15–20 wt% Pb+Zn (Si et al. 2013). The second largest orebody, the Danaotang orebody, is about 500 m long, 400 m wide, 0.1–20 m thick, and contains 2.5 Mt of sulfide ore grading 15–25 wt% Pb+Zn (Si et al. 2013). Recent mining exposures at the Fule deposit have revealed several mid-sized orebodies at depth and in the surrounding areas: No. 08 (400 m × 200 m × 2–12 m), No. 904 (340 m × 200 m × 1.5–15 m) and No. 74 veined orebody (200 m × 150 m × 3–15 m). These newly discovered orebodies together contain 2.0 Mt of sulfide ore with an average ore grade of 15–20 wt.% Pb+Zn (up

to 60 wt.%). Detailed field observations indicate that the metal grades of the orebodies correlate with the distance from the fault (Li et al. 2020b). High grades (up to 60 wt.% of Pb+Zn) of Zn-Pb orebodies mainly occurred proximal to the main faults (NS-trending F_{1-4} faults). The uppermost parts of the orebodies near the Kuaizehe river are intensely oxidized, accounting for around 25 vol% of the total metal ores. The sulfide minerals in the Fule deposit include sphalerite (dominant), galena, pyrite, and tennantite with minor chalcopyrite, accompanied by willemite, smithsonite, fine-grained cerussite, and minor hematite and greenockite as the supergene oxidized minerals (Figs. 2–4). Non-metallic minerals include primarily hydrothermal dolomite and calcite.

The Fule deposition model has been extensively reviewed by Zhou et al. (2018) and additional fluid inclusion and stable isotopic studies were carried out by several studies (Zhu et al. 2018; Li et al. 2019; Liu et al. 2021). Accordingly, the mineral parageneses in both the Fule and Fusheng mining areas are similar. The main stages of mineralization correspond to development of hydrothermal sulfides (pyrite, sphalerite, galena, Cu-bearing minerals) and carbonate (hydrothermal dolomite and calcite). The ore-fluid of this stage is characterized by middle-high salinity H_2O-NaCl fluids (5–16 wt.% NaCl eq.) of 120–210°C (Li et al. 2019). Later mineralizing stage corresponded to a waning of hydrothermal stage with development of carbonate minerals, only a few sulfides formed during this stage (Zhou et al. 2018). Metal precipitation in hydrothermal stage is controlled by the mixing of two fluids: a reducing S-rich fluid derived from host rocks (supported by S isotope evidence; Zhou et al. 2018; Li et al. 2019) and a metal-rich fluid originating from the basement (supported by Pb-Ge-Cd isotopes; Zhou et al. 2018; Zhu et al. 2018, and Liu et al. 2021). The study of supergene mineralization has not received much attention, only a few authors have identified several oxidized minerals, such as smithsonite, hematite, and cerussite (Zhou et al. 2018; Li et al. 2019).

SAMPLING AND ANALYTICAL METHODS

Sampling

A total of 100 ore samples were collected from the Fule deposit during several field mapping campaigns over the past five years. Most ore samples were collected from different mine levels of the Fule and Fusheng mining areas; some were also collected from drillcore intersections and the ore stockpile of the Fusheng ore blocks. Eight samples representative of the whole mining area were selected for detailed textural and micro-chemical investigation (see Table A1 for details). For each of the eight samples, one-inch-diameter polished blocks and/or thin sections were prepared and were investigated using an optical microscope, and a JSM-7800F (JEOL, Japan) scanning electron microscope (SEM) equipped with a back-scattered electron (BSE) detector and energy dispersive X-ray (EDX) spectrometer before further analyses.

Electron probe microanalysis

Quantitative mineral composition analyses were conducted using a JXA8530F-plus Electron Probe Microanalyzer at the State Key Laboratory of Ore Deposit Geochemistry (SKLODG), Institute of Geochemistry, Chinese Academy of Sciences (IGCAS), China. All measurements were performed at an accelerating voltage of 25 kV, beam current of 10 nA and beam size of 1–10 μm. The standards and measured spectral lines for each element are Si (willemite, Kα), S (sphalerite, Kα), Mn (willemite, Kα), Fe (chalcopyrite, Kα), Cu (chalcopyrite, Kα), Zn (sphalerite, Kα), Ge (germanium, Kα), As (arsenopyrite, Lα), Ag (sliver, Lα), Cd (cadmium, Lα), Sb (stibnite, Lα). Minimum detection limits were (2σ, in μg/g): Si (618), S (152), Mn (226), Fe (280), Cu (388), Zn (400), Ge (372), As (726), Ag (270), Cd (250) and Sb (306). The full list of analyzed elements are given in Supplementary Data (SD) 1.

Laser ablation-inductively coupled plasma mass spectrometry multi-elements analysis and element mapping

Trace element compositions of sulfides were determined using a Coherent COMPex Pro ArF 193 nm wavelength Excimer laser coupled with an Agilent 7700 Quadrupole mass spectrometer at the ARC Centre of Excellence in Ore Deposits (CODES), University of Tasmania, Australia. Spot analyses were performed with 26-µm-diameter spot size, 5 Hz pulse frequency and 3 J/cm^2 fluence. Each spot analysis includes 30 s of background measurement and 60 s laser-on-sample analysis. Standard reference materials used were STDGL2b2 (Danyushevsky et al. 2011) and GSD-1G (USGS) for determining concentrations of trace elements in sphalerite, pyrite, galena, and tennantite. The following isotopes were monitored: ^{34}S, ^{55}Mn, ^{57}Fe, ^{59}Co, ^{60}Ni, ^{65}Cu, ^{66}Zn, ^{72}Ge, ^{74}Ge, ^{75}As, ^{77}Se, ^{107}Ag, ^{111}Cd, ^{115}In, ^{118}Sn, ^{121}Sb, ^{205}Tl, ^{208}Pb and ^{209}Bi. Data reduction was done using the LADR software (https://norsci.com/ladr/) with the following internal standards: ^{66}Zn for sphalerite, ^{57}Fe for pyrite, ^{65}Cu for tennantite, and ^{208}Pb for galena. Average Zn concentrations for each sphalerite generation and Cu for tennantite were taken from EPMA measurements. Stoichiometric concentrations of Fe and Pb were respectively used for pyrite and galena.

Trace element data of carbonate (hydrothermal dolomite, calcite, smithsonite) and silicate minerals (willemite) and elemental maps were obtained using a RESOlution 193nm ArF excimer laser ablation system coupled with an Agilent 7500x quadrupole ICPMS at the SKLODG, IGCAS (China). Spot analyses were performed with an energy density of ~3 J/cm^2, and spot sizes varying from 26 to 40 µm to avoid ablating mineral inclusion. Standard reference materials used as external standards were NIST 610 and GSE-1G (USGS). The following isotopes were monitored during each measurement (30 s background, 50 s ablation):^{25}Mg, ^{29}Si, ^{34}S, ^{43}Ca, ^{55}Mn, ^{57}Fe, ^{59}Co, ^{60}Ni, ^{65}Cu, ^{66}Zn, ^{72}Ge, ^{74}Ge, ^{75}As, ^{77}Se, ^{107}Ag, ^{111}Cd, ^{115}In, ^{118}Sn, ^{121}Sb, ^{205}Tl, ^{208}Pb and ^{209}Bi. Instrumental drift corrections and elemental content calculations were performed with the ICPMSDataCal software (Liu et al. 2008), using ^{43}Ca signal as the internal standard for hydrothermal dolomite and calcite,

and ^{66}Zn and ^{29}Si for smithsonite and willemite, respectively. Average Si concentrations for each sample were taken from EPMA measurements for willemite. Stoichiometric Zn and Ca concentrations were used for smithsonite and carbonate minerals.

LA-ICPMS element mapping was carried out by ablating sets of parallel lines across the target minerals using an energy density of ~3 J/cm^2, spot size of 7–9 μm, scan speed of 9 to 16 μm/s (depending on the spot size) and a 10 Hz repetition rate. The same isotopes were analyzed as for the spot analyses. Identical rasters were done on the reference material of STDGL3, NIST 610 and GSE-1G at the start and end of each mapping run to correct for instrumental drift. Elemental concentration maps were compiled and processed using the Iolite software (Paton et al. 2011). All LA-ICPMS maps were produced for each element using a logarithmic color scale.

Isobaric interferences on Ge in the mass spectrometer may prevent the measurement of accurate Ge concentrations (Cook et al. 2009). However, previous studies have confirmed that interferences commonly have an insignificant effect on Ge measurements, even in Fe-rich, Ge-poor sphalerite (Frenzel et al. 2022). For Fe-/O-bearing minerals, two Ge isotopes (^{72}Ge and ^{74}Ge) were chosen for comparative analysis. The inferences of $^{56}Fe^{16}O$ and $^{58}Fe^{16}O$ on ^{72}Ge and ^{74}Ge, respectively, were monitored by comparing the measured abundance ratio of $^{72}Ge/^{74}Ge$ in the Fule sample to the natural ratio (0.77). If significant deviations of $^{72}Ge/^{74}Ge$ are >50% relative to 0.77, the measurement was considered as below the minimum detection limit (mdl), with the highest of two reported concentrations as the mdl. Spurious concentrations produced by the interference of Fe–O species on Ge never exceeded~0.5 μg/g.

Data treatment

The nature of data, sampling, and analysis processes can limit the applicability of specific statistical methods. Our data treatment procedures had two main purposes: (i) obtaining accurate

results for widely skewed dependent variables, and (ii) adjusting LA-ICPMS data to precisely reflect element partitioning behavior, regardless of the number of samples, minerals, or analyzed spots. Both procedures are necessary to ensure comparability between mineral chemistries.

High variability is an inherent trait of LA-ICPMS data. To address this issue, statistical results were determined using the geometric mean due to its reduced sensitivity to extreme outliers compared to the arithmetic mean. Additionally, we use the 95% confidence interval (CI), which was computed by adding or subtracting the standard deviation of the logarithm of the arithmetic mean logarithm of the data. This approach helped assess the precision of statistical estimates.

When studying trace elements in minerals, it is crucial to consider the hierarchical data structures (Dimitrijeva et al. 2018; Frenzel et al. 2022). LA-ICPMS data is often unbalanced due to the limited availability of geological samples, resulting in unequal numbers of observations at different hierarchical levels. To minimize the effect of samples, we discuss the element partitioning behavior following the order of "analysis spot" < "mineral generation" < "sample". The adjustment procedures are standard in Dimitrijeva et al. (2018).

RESULTS

Petrography and mineralogy

The paragenetic sequence in all investigated samples is similar (Fig. A1). The hydrothermal mineralization process is defined primarily through three different sphalerite generations, as summarized in Figure 5. Sulfides deposited during the three stages are texturally distinct, and sphalerite exhibits marked compositional differences (see below). Sphalerite and galena occur across the hydrothermal stage and are the major sulfides of the Fule deposit, accounting for ~35 vol% and 15 vol% of the total sulfide ores, respectively. In the supergene stages, willemite serves as the predominance ore mineral, accounting for ~50 vol% of the total oxides, accompanied with

smithsonite, cerussite and hematite (<20 vol%; see Table A1 for detail).

Stage 1

Pyrite 1 (Py1) is the earliest hydrothermal mineral in the entire hydrothermal process and is abundant in this stage. This pyrite is fine- to medium grained (<500 μm in diameter) irregular shape and commonly forms replacement and wrapping textures (Fig. 3A). In some cases, Py1 is replaced by tennantite, forming irregular, corroded grain boundaries (Fig. 3B). Sphalerite from this stage is represented by mm-sized anhedral crystals containing abundant discontinuous trails of inclusions, mostly of chalcopyrite with trace galena (Fig. 3A–3D). Two subtypes of sphalerite 1 (Sp1) are defined based on its co-existing mineral assemblage and color (Fig. 3C). Sphalerite 1a (Sp1a) is characterized by red-brown in color and replaces or encloses irregular-shaped Py1 (Figs. 3A and 3C). In some cases, tennantite replaces/corrodes Py1 and Sp1a (Fig. 3B). Sphalerite 1b (Sp1b) is red- to light-brown in color (Figs.3C and 3E) and overgrown by galena and/or tennantite (Figs. 3C and 3D). Tennantite exhibits replacement texture and forms veins crosscutting through the earlier sulfides of this stage (Figs. 3B and 3D). This mineral frequently replaces Py1 and Sp1b (Fig. 3B). Locally, tennantite and galena 1 (Gn1) form discontinuous veins (Fig. 3D). This galena occurs as replacement texture (Fig. 3B). In some samples, tennantite-galena veins crosscut the early Sp1b (Fig. 3D).

Stage 2

Sphalerite 2 (Sp2) is yellow- to light-yellow in transmitted-light, showing visible boundaries with Sp1b (Fig. 3E). It is free of mineral inclusions and can thus be easily distinguished from Sp1 (Figs. 3E–3J). Two subtypes of Sp2 are recognized based on the co-existing minerals. Sphalerite 2a (Sp2a) commonly present as coarser (>1mm in diameter), anhedral crystals, which are filled with galena in cavities and/or fractures (Figs. 3F and 3G) or are replaced by galena, exhibiting irregular contact boundaries (Fig. 3H). Sphalerite 2b (Sp2b) occurs with variable grain diameters, from fine-

(<50 μm) to coarse-grained (>500 μm) (Figs. 3I and 3J), accompanied by fine-grained pyrite 2 (Py2) and minor galena 2 (Gn2). This sphalerite is early compared to fine-grained Py2 aggregates (Figs. 3I and 3J). Galena 2, characterized by a grain size from approximately 100 μm to almost 2 mm (Figs. 3F and 3H), fills fractures within earlier sphalerite (Sp2a; Fig. 3G). This galena commonly replaces Sp2a, and the relic textures suggest that Gn2 is a later formation compared to Sp2a (Fig. 3H). Locally, fine-grained Gn2 grains infill in the pre-existing cavities of Sp2a (Fig. 3F). Pyrite 2 is fine-grained (<10 μm) and often forms larger aggregates (Figs. 3I and 3J). This pyrite frequently occurs on the edges of Sp2b crystals (Fig.3I), indicating that Py2 is typically formed later than Sp2b. In addition, the abundance of hydrothermal dolomite 1 (HD1) fills in the vugs/voids between earlier sulfides (Figs. 3G–3J).

Stage 3

Sphalerite 3 (Sp3) is present as separate grains/inclusions within coarsely crystalline galena 3 (Gn3) (Figs. 3K and 3L). It forms grains of various shapes and sizes, primarily quadrangular and elliptic oval shapes (50–200 μm in diameter; Fig. 3K). Galena 3 occurs as mm-sized grains and commonly encloses and replaces Sp3 (Figs. 3K and 3L). Such texture suggests it is late compared to Sp3. Hydrothermal dolomite 2 (HD2) is abundant in this stage and is accompanied by previously described minerals, i.e., sphalerite and galena (Fig. 3L). Calcite is generally the very last mineral and crosscuts previous sulfides (Fig. 3D) or infills sulfide fractures (Fig. 3J).

Supergene stage

Willemite is the dominant mineral of this stage, confirmed by EPMA (SD 1). More importantly, the mineral is co-genetic with the minerals typically recognized as supergene (Fig. 4), together with trace element signatures (see below), therefore confirming its supergene origin (Mondillo et al. 2020). Willemite generally directly replaces original sphalerite/smithsonite with irregular boundary edges

(Figs. 4A–4B). Locally, the mineral encloses the separate grains of hematite, cerussite, and apatite, indicating willemite typically formed later than these minerals (Figs. 4C–4F). Smithsonite occurs as the replacement textures (Figs. 4B and 4D) that is commonly replaced by willemite (Fig.4B). In some cases, smithsonite intergrows with hematite and willemite (Fig. 4D). Cerussite and greenockite typically distribute among the grain margin of galena and sphalerite (Figs. 4E and 4F). In some case, greenockite-cerussite aggregates fill in the willemite stockwork (Fig. 4A). Locally, cerussite presents as separate grains/inclusions that infills the pre-existing cavities (Figs. 4B). Hematite is generally replaced by willemite (Fig. 3C) or infills the cavities and voids of pre-existing minerals (Figs. 4B and 4D).

Mineral chemistry

LA-ICPMS trace element data

Minor and trace element results of sphalerite are summarized in Table A2. The elements not shown in Table A2 are largely hosted by inclusions (e.g., Pb) or mostly below or around mdl (e.g., In, Sn, Se, Bi). It is apparently difference in texture, mineral association, and compositional among different types of sphalerite (Figs. 5 and 6). When all subtypes/generations occur in the same sample, concentrations of Ge and Cu generally decrease from Sp1 to Sp3, while concentrations of Cd, Fe, and Mn show the opposite behavior. Cobalt, Ni, and Tl concentrations, on the other hand, do not show clear systematic differences between three sphalerite generations (Table A2). Another interesting observation is that As, Ag, and Sb concentrations fluctuate, displaying first an increase and then a decrease from Sp1 to Sp3 (Fig. 6).

Minor and trace elements of other sulfides (pyrite, tennantite, galena), together with corresponding sphalerite covering all hydrothermal stages are summarized in Table A3 (full dataset in SD 2) and presented in Figure 7. In all analyzed samples, compared with sulfides within each

stage, sphalerite had the highest concentrations of Ge and Cd, while having the lowest concentrations of Sb and Tl. Nickel concentration is typically elevated in pyrite, while Tl is highest in galena, and Ag, As and Sb are naturally enriched in tennantite. Relative to other sulfides, the lowest concentrations of Ge, Ni, As and Co were measured in galena, and the lowest Ag and Cd concentrations in pyrite (Fig. 7). Surprisingly, Py1 contains detectable Ge concentrations in sample FL1536-27, ~26 ug/g on average (up to 217 ug/g Ge; SD 2).

Hydrothermal dolomite and calcite co-existing with sulfides contain extremely low Ge concentrations (<0.65 μg/g; SD 2), with no significant difference across samples or ore stage. Most of analyzed spots are below or around mdl, and the spots with measurable Ge are largely attributed to microscale inclusions of sphalerite due to Ge-Zn peaks occurring together in the LA-ICPMS ablation signals (Fig. A2).

Supergene minerals, including willemite and smithsonite, and corresponding original sphalerite are summarized in Table A4 and presented in Figure A3. The small grain sizes (<20 μm) of hematite, cerussite, and greenockite hindered compositional analysis. In all analyzed spots, Fe, Mn, Co, Cu, Ge, Cd, Sb, and As are measurable in willemite and smithsonite, but some of them such as Fe, Mn, Co, Cu, Cd, and Sb, are significantly lower than that in the original sphalerite when comparing the mass ratios of minor/trace elements with Zn (Fig. A3).

LA-ICPMS element mapping

The first set of element maps highlighting the pyrite (Py1)-sphalerite (Sp1a)-tennantite-galena-dolomite assemblages (sample 1536-27; Fig. 8) confirm that Ge and Cd are preferentially enriched in sphalerite whereas the preferred host for Co, Ni, and Tl is pyrite. Surprisingly, pyrite, to some extent, concentrates substantial Ge. Copper, As, Ag, and Sb are predominantly concentrated in the tennantite. Hydrothermal dolomite is relatively barren of minor/trace elements but does contain abundant Mn

relative to other minerals. Distributions of Co, Ni, Tl, and possible Ge display extensive heterogeneity within single pyrite grain. The grain boundaries of sphalerite and tennantite exhibit low concentrations of Tl.

The second set of elements maps on sphalerite (Sp2b)-pyrite (Py2)-dolomite assemblages (sample FL-3; Fig. 9) indicate that sphalerite is relatively enriched in Co, Cu, Cd, Ge, Sb and mostly Ag. Meanwhile, Fe, Ni, and As are preferentially hosted in pyrite. Manganum is enriched in abundance in hydrothermal dolomite compared to other minerals. Note here that Cu, Ge, Sb, and possibly Ag display a similar zonation pattern within the sphalerite grain.

The third set of elemental maps (sample FL18-4; Fig. 10), including sphalerite and willemite, shows that sphalerite primarily hosts Mn, Co, Fe, Cd and Cu whereas willemite concentrates As. Germanium and Sb, in this case, are not solely concentrated in sphalerite but also preferentially enriched in willemite. Compositional zoning of Cu, Ge, and Cd are observed in the sphalerite; external zones of the grain are enriched in Cu and Ge, while Cd seems to show the opposite behavior. The correlation between Ge and Cu/Cd is absent in willemite compared to sphalerite. Selenium is observed to be concentrated in the grain boundaries of willemite and sphalerite, whilst Sb displays an erratic distribution in both sphalerite and willemite grains.

The last set of elemental maps on smithsonite-willemite assemblages (sample FL-15-2; Fig. 11) and indicated that smithsonite is the preferential host for Mg, Co, and Cd, while willemite relatively concentrates Ge, Se, As, and Sb. All elements are distributed heterogeneously in the LA-ICPMS maps. Small inclusions of greenockite and hematite were found; the former is enriched Cd, while the latter is noted Ge and Sb (Fig. 11).

DISCUSSION

Germanium deportment in MVT sulfides

Many studies have documented the elemental partitioning behavior between co-crystallized sphalerite, galena, and chalcopyrite/pyrite (e.g., George et al. 2016; Xu et al. 2020; Wei et al. 2021 and references therein). However, concentrations of Ge and its partitioning among different sulfides are overlooked. Here, the main sulfides in MVT deposits were analyzed, attempting to reveal Ge partitioning in MVT sulfides, even if equilibrium crystallization is not necessarily implied.

In the Fule MVT deposit, all LA-ICMPS spot and mapping analyses show that the highest Ge concentrations are recorded in sphalerite (Figs. 7–9), indicating Ge is preferentially partitioned into sphalerite relative to pyrite, tennantite, and galena. Considering Ge concentrations and mineral proportions (>35 vol%), sphalerite is thus probably the primary host of Ge in Fule sulfide ores. The second most Ge-rich sulfide in Fule appears to be pyrite. It always contains more Ge than galena and tennantite (Fig. 7). Some pyrite (e.g., sample 1536-27) exhibit flat Ge signal spectra (Fig. A2), yet still maintaining high concentrations of Ge (mean 14.2 μg/g; up to 217 μg/g; SD 2). The values, while not surprising, are lower than those present in co-crystallized sphalerite (mean 43.9 μg/g; up to 797 μg/g). Such partitioning behavior is also verified by LA-ICMPS elemental maps (Fig. 8) and the dataset of previous study (Li et al. 2019). Notable, the Fule pyrite contains more Ge than previously reported results of other deposits elsewhere (mostly <2 μg/g; Vincent et al. 2021; Frenzel et al. 2022; Zhu et al. 2022; Li et al. 2023). It is thus expected that pyrite may have a more significant role in controlling the distribution of trace Ge in certain deposits than previously acknowledged, although the nano occurrence mode of Ge remains undisclosed. If pyrite volume greatly exceeds that of sphalerite, it is plausible that pyrite could potentially serve as the primary host for Ge. While pyrite in Fule is volumetrically minor, it is thus only a minor Ge host. Germanium concentrations in Fule tennantite are commonly <5 μg/g (SD 2), and lower than sphalerite and pyrite from same ore stage (Fig. 7). Low Ge concentrations in tennantite are also confirmed by LA-ICPMS elemental maps (Fig.

8). Tennantite thus is a poor Ge-carrier in Fule. EPMA studies of galena from the Fagundes and Ambrósia deposits, Brazil found an uncommon abundance of Ge (up to 8470 μg/g), exceeding concentrations measured in sphalerite (Monteiro et al. 2006). We anticipated that Fule galena exhibit measurable Ge concentrations. However, Fule galena has the lowest concentrations of Ge (typically <0.2μg/g, SD 2) compared to sphalerite, pyrite, and tennantite. Similar results are also revealed in the sphalerite-galena±pyrite assemblages of other MVT deposits from South China and East Belgium (e.g., Hu et al. 2019, 2021; Baele et al. 2021; Wei et al. 2021). Our study confirmed the fact that galena is significantly depleted in Ge, and therefore cannot serve as the primary Ge host. Chalcopyrite is uncommon in MVT deposits, only occurring in specific environments (Leach et al. 2005). In Fule, chalcopyrite is associated with sphalerite (Figs. 3A–3E and 5), but it is difficult to assess the partitioning of Ge between sphalerite and chalcopyrite due to the small sizes of chalcopyrite that render trace element analysis by LA-ICPMS impossible. It is noted that, in the Tianbaoshan MVT Zn-Pb(-Cu) deposit, Ge is predominantly hosted in sphalerite, despite abundant chalcopyrite being present (Ye et al. 2016). However, recent studies found that chalcopyrite serves as the major Ge-carrier in Cu-dominant sulfide deposits (Belissont et al. 2019; Foltyn et al. 2022). Further study is thus required to reveal why chalcopyrite acts as a significant Ge-carrier in certain deposits, even in the presence of sphalerite.

The diversity of Ge concentrations in sphalerite carries important ramifications for better revealing the distribution of Ge in sphalerite. In Fule sphalerite, spot concentrations for Ge have a wide range (<0.5–797 μg/g, SD 2). Interestingly, sphalerite with distinct textural association contains markedly different Ge concentrations (Figs. 5 and 6). From early to late ore stages, there is a general decrease in Ge concentrations; the highest Ge concentrations are measured in the Sp1a (enclosed pyrite), and the lowest Ge concentrations are found in tiny sphalerite grains within Gn3 (Fig. 7).

Importantly, there is a well-defined correlation between Ge and Cu along the (Ge/Cu) = 1/2 line (Fig. 12), consistent with Ge–Cu correlations observed in previous studies (Ye et al. 2016; Wei et al. 2019; Cugerone et al. 2021, Fougerouse et al. 2023 and references therein). It seems reasonable to expect that Ge is incorporated into sphalerite lattice though $3Zn^{2+} \leftrightarrow Ge^{4+} + 2Cu^{+}$, though Ge-Cu submicron-inclusions could not be completely ruled out. Strong chalcophilic nature of Ge suggests that increased Cu levels are essential for enhancing Ge concentrations in sphalerite (Belissont et al. 2016). The increased fluid activity of Cu has the potential to strengthen Ge-Cu bonds and, consequently, lead to the incorporation of more Ge in precipitating sphalerite (Wei et al. 2019).

Elemental partitioning among MVT sulfides

In addition to Ge, we first examined the partitioning behavior of several elements on the sphalerite-pyrite-tennantite-galena assemblage. Without exception, all analyzed tennantite samples have high concentrations of As, Ag, and Sb relative to galena, pyrite, and sphalerite (Fig. 7), in agreement with the results of LA-ICMPS elemental maps (Fig. 8). When tennantite is present, As, Ag and Sb are preferentially incorporated into tennantite. As shown in Figure 7, tennantite generally contains more Ag and Sb than galena which, in turn, contains more Ag than sphalerite and pyrite, so that $Ag_{tennantite} > Ag_{galena} > Ag_{sphalerite} > Ag_{pyrite}$. While pyrite contains more Sb than sphalerite (Fig. 7), so that $Sb_{tennantite} > Sb_{galena} > Sb_{pyrite} > Sb_{sphalerite}$. Arsenic displays obviously different partitioning behavior compared to Sb and Ag, in which tennantite commonly contains more As than pyrite which, in turn, contains more As than sphalerite and galena, so that $As_{tennantite} > As_{pyrite} > As_{sphalerite} > As_{galena}$. Our data also confirmed that Py1 preferentially incorporates Co, Ni, and Tl relative to Gn1, Sp1, and tennantite (Fig. 7), reflecting the fact that these elements readily enter the pyrite crystal structure (Large et al. 2009; Cook et al. 2013). However, in stage 2, Sp2 concentrates more Co relative to pyrite, i.e., $Co_{sphalerite} > Co_{pyrite}$ (Fig. 7). Low levels of Co in the later formed Py2, revealed by LA-

ICPMS elemental maps (Fig. 9), may attribute to the relatively low Co concentrations in late hydrothermal fluids. Cadmium concentrations in Fule sphalerite are comparable to those found in MVT sphalerite elsewhere (Cook et al. 2009; Ye et al. 2011; Frenzel et al. 2016; Hu et al. 2019, 2021; Torró et al. 2023 and references therein). As shown in Figure 7, sphalerite contains more Cd than tennantite and, in turn, pyrite and galena, so that $Cd_{sphalerite} > Cd_{tennantite} > Cd_{galena} > Cd_{pyrite}$. The preferred Cd partitioning behavior is also confirmed by the elemental maps (Figs. 8 and 9) and high Cd contents in sphalerite can be attributed to the CdS_2-ZnS_2 solid solution (Cherin et al. 1970).

Germanium and related elements mobility during weathering

Trace elements data, including Ge, have been conducted on the Fe-(oxy)hydroxides, hemimorphite, willemite, and related minerals (Saini-Eidukat et al. 2009; Choulet et al. 2017, 2019; Mondillo et al. 2018a, 2020 and references therein). However, the mobilization of Ge and related elements during supergene weathering still need be evaluated. Supergene minerals, including willemite and smithsonite, and corresponding original sphalerite were analyzed here, attempting to quantitatively evaluate the remobilization of Ge and related elements.

In the Fule MVT deposit, comparing the mass ratios of minor/trace elements to Zn, sphalerite usually contains more Fe, Mn, Co, Ge, and Sb than smithsonite, and more Fe, Mn, Co, Cu, Cd, and Sb than willemite (Fig. 13), indicating these elements are released during weathering. The opposite is true for As, Cu, and Cd in smithsonite and As in willemite (Fig. 13), indicating these elements are gained during weathering. LA-ICPMS data show qualitatively that sphalerite and willemite contain almost similar amounts of Ge (Fig. 13), though Ge distribution is heterogeneous both between and within mineral grains (Fig. 10). Comparing the quantitative results of Ge concentrations in sphalerite and willemite within same sample, there appears to be no apparent Ge loss. In sample FL18-15-2, for example, the concentrations of Ge in sphalerite and willemite average approximately 123 and 130

μg/g, respectively (Table A3). More importantly, similar mass ratios of Ge/Zn in sphalerite and willemite within same sample are seen to suggest that Ge together with Zn is re-incorporated into the willemite during weathering (Choulet et al. 2019). Germanium in willemite occurs as Ge^{4+} and is tetrahedrally coordinated with oxygen, indicating that it substitutes for Si rather than Zn (Saini-Eidukat et al. 2016). Similar conclusions were also reported in many Zn-silicate deposits worldwide (e.g., Choulet et al. 2017, 2019; Mondillo et al. 2018b).

Mineralogical host of Ge in weathering products

To quantify which minerals host Ge in weathering products, it is necessary to determine the mineralogical makeup and Ge concentrations in all relevant minerals. As shown in Table A1, willemite accounts for >50% of the total oxide ores with minor amounts of smithsonite (<5%), Fe-hydroxides (<5%), and trace cerussite (<1%). In these supergene minerals, Ge concentrations in willemite range from 0.48 μg/g to 448 μg/g (SD 3), which is two or more orders of magnitude greater than that in smithsonite (<mdl to 2.56 μg/g; SD 3). Noteworthy, Ge also enriched in Fe-(oxy)hydroxides, such as hematite and goethite (Bernstein et al. 1985; Melcher 2003; Mondillo et al. 2018a,b; Santoro et al. 2020). At the Apex mine in southwest Utah, USA, for example, high contents of Ge are reported in goethite (up to 5310 μg/g) and hematite (up to 7000 μg/g; Bernstein et al. 1985). Fe-hydroxides from Tsumeb, Namibia, also incorporate large amounts of Ge (up to 2.5 wt.%; Melcher 2003). Interestingly, Fe-hydroxides are infrequent in Fule, constituting only 5% of the total volume of oxidized ores (Table A1). In addition, the incorporation of Ge in carbonate minerals are limited (Verhaert et al. 2017; Mondillo et al. 2018b), such as low contents of Ge in smithsonite (typically <0.2 μg/g; SD 3). Hence, willemite is a significant repository of Ge in the oxidized ores.

Control on the formation of willemite

Germanium redistribution in oxidized ores provides an indication of the geochemical conditions

prevailing at the time of sulfide weathering (Mondillo et al. 2018b). As mentioned earlier, Zn-silicate is the important host for Ge in Zn-oxide ores, largely attributed to Ge showing an affinity for Si and thus being incorporated into Zn-silicates rather than Zn carbonates during sulfide weathering (Mondillo et al., 2018b; Choulet et al. 2019; Withe et al. 2022; this study). Therefore, the formation of willemite controls how the abundance of Ge could be conserved during weathering.

Thermodynamic modeling showed the solubility of willemite greatly depends on pH, silica activity, and $fCO_{2(gas)}$ (McPhail et al. 2003; Reichert and Borg 2008). At 25°C, willemite is a stable phase relative to zinc carbonates under high pH (>7), high silica activity (quartz saturation), and low $fCO_{2(gas)}$ conditions (McPhail et al. 2003). pH and $fCO_{2(gas)}$ are probably buffered by carbonate-rich host rocks (McPhail et al. 2003; Reichert and Borg 2008). The quantitative precipitation of willemite and other zinc silicates mainly depends on the availability of silica (Reichert and Borg 2008; Choulet et al. 2017). The solubility of H_4SiO_4(aq) is relatively not very high in carbonate-buffered solutions (Dove and Rimstidt 1994). Conversely, the solubility of the silica phase increases significantly in such an environment, transitioning from crystalline quartz ($9.6*10^{-4}$ mol/l) to amorphous silica ($2.0*10^{-3}$ mol/l). The abundance of opal in the oxidation site is the primary factor that affects the formation of Zn-silicate (Reichert and Borg 2008).

The Emeishan basalt is expected to be the main local source of silica at Fule. The presence of opal in the Emeishan basalt, especially the volcaniclastics near the ore host rocks (e.g., Zhang 1999). The abundance of apatite aggregates occurs in the willemite veins (Fig. 4A). It is thus expected that meteoric solutions for sulfide weathering flow through silica-rich rocks. More importantly, the sulfide veins in the topmost orebodies are in direct contact with the opal-rich Emeishan basalt (Zhou et al. 2018). Hence, the dissolution of silica phase, especially opal, is reasonable to supply sufficient Si for the formation of willemite. The long-lived humid (sub)tropical climates since Late Permian,

especially Miocene to now could maintain high efficiency of supergene weathering (P. Li et al. 2020). Overall, the specific environment at Fule appears to prompt the formation of abundant willemite in the oxidized zone, preventing Ge dispersion during supergene overprinting. The redistribution of Ge from sphalerite to Zn-silicates (e.g., willemite) may be a potentially important process worldwide. In the present context of Ge criticality, revealing Ge distribution from sulfide deposition to oxidative weathering is vital for the assessment of the resource and recovery potential of Ge.

IMPLICATIONS

This systematic study of Ge distribution in the different mineral assemblage from the Fule Ge-bearing MVT deposit using a holistic approach provides new insight into understanding Ge geochemical behaviors in the low-*T* hydrothermal deposit and dictate metallurgical strategies for Ge recovery. Germanium is primarily hosted within sphalerite but each textural variety of sphalerite contains markedly distinct Ge concentrations. At the microscale, pyrite may incorporate subordinate amounts of Ge that may however be significantly greater than previously recognized, while galena and tennantite are both poor Ge-carriers. Copper, Sb, As, and Ag are noted in tennantite while Ni and Tl are preferentially incorporated into pyrite. Cobalt is mainly hosted in pyrite and sphalerite. Cadmium is essentially hosted in sphalerite. During weathering, Ge and related elements, such as Mn, Co, Fe, Cu, and Sb, are released from original sphalerite. Germanium is predominantly reincorporated into the willemite lattice, and the formation of abundant Zn-silicates appears to prevent the dispersion of Ge during weathering. In light of current Ge criticality, revealing Ge distribution from sulfide deposition to oxidative weathering provides insight into the assessment of the resource and recovery potential of Ge.

ACKNOWLEDGMENTS

This study was supported by the National Natural Science Foundation of China (92162218,

42173025, and U1812402), the Natural Science Foundation of Guizhou Province (Qiankehejichu[2021]123), Major collaborative innovation projects for prospecting breakthrough strategic action of Guizhou Province, China ([2022] ZD004) and Sino-German (CSC-DAAD) Postdoc Scholarship Program. The authors thank Hongliang Nian and Jinjun Cai for help in fieldwork and sample collection, Xiang Li for help with EPMA, and Ivan Belousov, Paul Olin, and Zhihui Dai for assistance with LA-ICPMS analyses. This paper benefited from the critical comments of Alexandre Cugerone, and Nicola Mondillo on an earlier version of the manuscript. Finally, we would like to thank Don Baker and Kimberly Tait, editors of *America Mineralogist*, and two reviewers, Walid Salama and Huan Li for their thorough reviews and insightful suggestions.

REFERENCES CITED

Baele, J.M., Bouzahzah, H., Papier, S., Decrée, S., Verheyden, S., Burlet, C., Pirard, E., Franceschi, G., and Dejonghe, L. (2021) Trace-element imaging at macroscopic scale in a Belgian sphalerite-galena ore using Laser-Induced Breakdown Spectroscopy (LIBS). Geologica Belgica, 24(3/4), 125–137.

Belissont, R., Boiron, M.C., Luais, B., and Cathelineau, M. (2014) LA-ICP-MS analyses of minor and trace elements and bulk Ge isotopes in zoned Ge-rich sphalerites from the Noailhac–SaintSalvy deposit (France): insights into incorporation mechanisms and ore deposition processes. Geochimica et Cosmochimica Acta, 126, 518–540.

Belissont, R., Muñoz, M., Boiron, M.C., Luais, B., and Mathon, O. (2016) Distribution and oxidation state of Ge, Cu and Fe in sphalerite by μ-XRF and K-edge μ-XANES: insights into Ge incorporation, partitioning and isotopic fractionation. Geochimica et Cosmochimica Acta, 177, 298–314.

Belissont, R., Munoz, M., Boiron, M.C., Luais, B., and Mathon, O. (2019) Germanium crystal chemistry in cu-bearing sulfides from micro-xrf mapping and micro-XANES spectroscopy. Minerals, 9(4), 227.

Bernstein, L.R. (1985) Germanium geochemistry and mineralogy. Geochimica et Cosmochimica Acta, 49(11), 2409–2422.

Cherin, P., Lind, E.L., and Davis, E.A. (1970) The preparation and crystallography of cadmium zinc sulfide solid solutions. Journal of the Electrochemical Society, 117(10), 233–236.

Choulet, F., Barbanson, L., Buatier, M., Richard, J., Vennemann, T., Ennaciri, A., and Zouhair, M. (2017). Characterization and origin of low-*T* willemite (Zn_2SiO_4) mineralization: the case of the Bou Arhous deposit (High Atlas, Morocco). Mineralium Deposita, 52,1085–1102.

Choulet, F., Richard, J., Boiron, M. C., Dekoninck, A., and Yans, J. (2019). Distribution of trace elements in willemite from the Belgium non-sulphide deposits. European Journal of Mineralogy, 31(5-6), 983-997.

Commission European (2023) Study on the Critical Raw Materials for the EU. 2023 Final Report. https://single-market-economy.ec.europa.eu/system/files/2023-03/Study%202023%20CRM%20Assessment.pdf

Cook, N.J., Ciobanu, C.L., Danyushevsky, L.V., and Gilbert, S. (2011) Minor and trace elements in bornite and associated Cu–(Fe)-sulfides: A LA-ICP-MS study. Geochimica et Cosmochimica Acta, 75, 6473–6496.

Cook, N.J., Ciobanu, C.L., Meria, D., Silcock, D., and Wade, B.P. (2013) Arsenopyrite-pyrite association in an orogenic gold ore: Tracing mineralization history from textures and trace elements. Economic Geology, 108, 1273–1283.

Cook, N.J., Ciobanu, C.L., Pring, A., Skinner, W., Shimizu, M., Danyushevsky, L., Saini-Eidukat, B., and Melcher, F. (2009) Trace and minor elements in sphalerite: A LA-ICPMS study. Geochimica et Cosmochimica Acta, 73(16), 4761–4791.

Cugerone, A., Cenki-Tok, B., Chauvet, A., Le Goff, E., Bailly, L., Alard, O., and Allard, M. (2018) Relationships between the occurrence of accessory Ge-minerals and sphalerite in Variscan Pb-Zn deposits of the Bossost anticlinorium, French Pyrenean Axial Zone: chemistry, microstructures and ore-deposit setting. Ore Geology Reviews, 95, 1–19.

Cugerone, A., Cenki-Tok, B., Muñoz1, M., Kouzmanov, K., Oliot, E., Motto-Ros, V., and Le Goff, E. (2021) Behavior of critical metals in metamorphosed Pb-Zn ore deposits: example from the Pyrenean Axial Zone. Mineralium Deposita, 56, 685–705.

Danyushevsky, L., Robinson, P., Gilbert, S., Norman, M., Large, R., McGoldrick, P., and Shelley, M. (2011) Routine quantitative multielement analysis of sulphide minerals by laser ablation ICP-MS: standard development and consideration of matrix effects. Geochemistry: Exploration, Environment, Analysis, 11, 51–60.

Dmitrijeva, M., Metcalfe, A.V., Ciobanu, C.L., Cook, N.J., Frenzel, M., Keyser, W.M., Johnson, G., and Ehrig, K. (2018) Discrimination and variance structure of trace element signatures in Fe-oxides: a case study of BIF-mineralisation from the Middleback Ranges, South Australia. Mathematical Geosciences, 50, 381–415.

Dove, P.M., and Rimstidt, J.D. (1994) Silica–water interactions. In: Heaney, P.J., Prewitt, C.T., Gibbs GV (Eds), Silica, Physical Behavior, Geochemistry and Materials Applications. Reviews in Mineralogy, 29, 259–308.

Fougerouse, D., Cugerone, A., Reddy, S.M., Luo, K., and Motto-Ros, V. (2023) Nanoscale distribution of Ge in Cu-rich sphalerite. Geochimica et Cosmochimica Acta, 346, 223–230.

Foltyn, K., Erlandsson, V.B., Zygo, W., Melcher, F., and Pieczonka, J. (2022). New perspective on trace element (Re, Ge, Ag) hosts in the Cu-Ag Kupferschiefer deposit, Poland: Insight from a LA-ICP-MS trace element study. Ore Geology Reviews, 143, 104768.

Frenzel, M., Hirsch, T., and Gutzmer, J. (2016) Gallium, germanium, indium, and other trace and minor elements in sphalerite as a function of deposit type — A meta-analysis. Ore Geology Reviews, 76(9), 52–78.

Frenzel, M., Mikolajczak, C., Reuter, M.A., and Gutzmer, J. (2017) Quantifying the relative availability of high-tech by-product metals – The cases of gallium, germanium and indium. Resources Policy, 52, 327–335.

Frenzel, M., Voudouris, P., Cook, N.J., Ciobanu, C.L., Gilbert, S., and Wade, B.P. (2022) Evolution of a hydrothermal ore-forming system recorded by sulfide mineral chemistry: a case study from the Plaka Pb–Zn–Ag Deposit, Lavrion, Greece. Mineralium Deposita, 57, 417–438.

Gagnevin, D., Menuge, J.F., Kronz, A., Barrie, C., and Boyce, A.J. (2012) Minor Elements in Layered Sphalerite as a Record of Fluid Origin, Mixing, and Crystallization in the Navan Zn-Pb Ore Deposit, Ireland. Economic Geology, 109, 1513–1528.

George, L., Cook, N.J., and Ciobanu, C.L. (2016) Partitioning of trace elements in co-crystallized sphalerite-galena- chalcopyrite hydrothermal ores. Ore Geology Reviews, 77, 97–116.

Höll, R., Kling, M., and Schroll, E. (2007) Metallogenesis of germanium—a review. Ore Geology Reviews, 30(3-4),145–180.

Hu, Y.S., Ye, L., Huang, Z.L., Li, Z.L., Wei, C., and Danyushevsky, L. (2019) Distribution and existing forms of trace elements from Maliping Pb-Zn deposit in Northeastern Yunnan, China: A LA-ICPMS study. Acta Petrologica Sinica, 35(11), 3477–3492 (in Chinese with English abstract).

Hu, Y.S., Wei, C., Huang, Z.L., Danyushevsky, L., and Wang, H.Y. (2021) LA-ICP-MS sphalerite and galena trace element chemistry and mineralization-style fingerprinting for carbonate-hosted Pb-Zn deposits: Perspective from early Devonian Huodehong deposit in Yunnan, South China. Ore Geology Reviews, 136, 104253.

Johan, Z. (1988) Indium and Germanium in the structure of sphalerite: an example of coupled substitution with copper. Mineralogy and Petrology, 39, 211−229.

Large, R.R., Danyushevsky, L., Hollit, C., Maslennikov, V., Meffre, S., Gilbert, S., Bull, S., Scott, R., Emsbo, P., Thomas, H., Singh, B., and Foster, J. (2009) Gold and trace element zonation in pyrite using a laser imaging technique: Implications for the timing of gold in orogenic and Carlin-style sediment-hosted deposits. Economic Geology 104: 635–668

Li, H., Wang, C., Zhu, D.P., and Jiang, W.C. (2021) Metallogenic environment of skarn-type and vein-type Pb-Zn ore body in the Huangshaping deposit and its implications of deep deposit exploration. The Chinese Journal of Nonferrous Metals. 33(2), 630−651.

Li, H., Zhu, D.P., Algeo, T.J., Li, M., Jiang, W.C., Chen, S.F., and Elatikpo, S.M. (2023) Pyrite trace element and S-Pb isotopic evidence for contrasting sources of metals and ligands during superimposed hydrothermal events in the Dongping gold deposit, North China. Mineralium Deposita, 58, 337−358.

Li, J.W., Li T.J., Jia, H.X., and Wang, A.J. (2023) Determination of China's Strategic and Critical Minerals List. Acta Geoscientica Sinica, 44(2), 261–270

Li, P., Zhang, C., Kelley, J., Deng, C., Ji, X., Jablonski, N.G., Wu H.B., Fu Y., Guo, Z.T., and Zhu, R. (2020). Late Miocene climate cooling contributed to the disappearance of hominoids in Yunnan region, southwestern China. Geophysical Research Letters, 47(11), e2020GL087741.

Li, Z.L., Ye, L., Hu, Y.S., Wei, C., Huang, Z.L., Nian, H.L., Cai, J.J., and Danyushevsky, L. (2019) The trace (dispersed) elements in pyrite from the Fule Pb-Zn deposit, Yunnan Province, China, and its genetic information: A LA-ICPMS study. Acta Petrologica Sinica, 35(11), 3370–3384 (in Chinese with English abstract).

Li. Z.L., Ye, L., Hu, Y.S., Wei, C., Huang, Z.L., Yang, Y.L., and Danyushevsky, L. (2020a) Trace elements in sulfides from the Maozu Pb-Zn deposit, Yunnan Province, China: Implications for trace-element incorporation mechanisms and ore genesis. American Mineralogist, 105, 1734–1751.

Li, Z.L., Ye, L., Hu, Y.S., Huang, Z.L., Wei, C., and Wu, T. (2020b) Origin of the Fule Pb–Zn deposit, Yunnan Province, SW China: insight from in situ S isotope analysis by NanoSIMS. Geological Magazine, 157, 393–404.

Liu, Y.S., Hu, Z.C., Gao, S., Günther, D., Xu, J., Gao, C.G., and Chen, H.H. (2008) In situ analysis of major and trace elements of anhydrous minerals by LA-ICP-MS without applying an internalstandard. Chemical Geology, 257, 34–43.

Lockington, J.A., Cook, N.J., and Ciobanu, C.L. (2014) Trace and minor elements in sphalerite from metamorphosed sulphide deposits. Mineralogy and Petrology, 108, 873–890.

McPhail, D.C., Summerhayes, E., Welch, S., and Brugger, J. (2003) The Geochemistry of Zinc in the Regolith. I.C. Roach (Ed.), Advances in Regolith. CRC for Landscape Environments and Mineral Exploration, 287–291.

Melcher, F. (2003): The Otavi Mountain Land in Namibia: Tsumeb, germanium and snowball earth. Mitt. Österreich. Mineral.Gesell., 148, 413–435.

Möller, P. (1987) Correlation of homogenization temperatures of accessory minerals from sphalerite-bearing deposits and Ga/Ge model temperatures. Chemical Geology, 61,153–159.

Mondillo, N., Arfè, G., Herrington, R., Boni, M., Wilkinson, C., and Mormone, A. (2018a) Germanium enrichment in supergene settings: evidence from the Cristal nonsulfide Zn prospect, Bongará district, northern Peru. Mineralium Deposita, 53,155–169.

Mondillo, N., Herrington, R., Boyce, A.C., Wilkinson, C., Mormone, A., Santoro, L., and Rumsey, M. (2018b) Critical elements in non-sulfide Zn deposits: a reanalysis of the Kabwe Zn-Pb ores (central Zambia). Mineralogical Magazine, 82(S1), S89–S114.

Mondillo, N., Accardo, M., Boni, M., Boyce, A., Herrington, R., Rumsey, M., and Wilkinson, C. (2020) New insights into the genesis of willemite (Zn_2SiO_4) from zinc nonsulfide deposits, through trace elements and oxygen isotope geochemistry. Ore Geology Reviews, 118, 103307.

Monteiro, L.V.S., Bettencourt, J.S., Juliani, C., and de Oliveira, T.F. (2006) Geology, petrography, and mineral chemistry of the Vazante non-sulfide and Ambrósia and Fagundes sulfide-rich carbonate-hosted Zn–(Pb) deposits, Minas Gerais, Brazil. Ore Geology Reviews, 28(2), 201-234.

Murakami, H., and Ishihara, S. (2013) Trace elements of indium-bearing sphalerite from tin-polymetallic deposits in Bolivia, China and Japan: a femto-second LA-ICPMS study. Ore Geology Reviews, 53, 223–243.

Paton, C., Hellstrom, J., Paul, B., Woodhead, J., and Hergt, J. (2011) Iolite: Freeware for the visualization and processing of mass spectrometric data. Journal of Analytical Atomic Spectrometry, 26 (12), 2508–2518.

Pfaff, K., Koenig, A., Wenzel, T., Ridley, I., Hildebrandt, L.H., Leach, D.L., and Markl, G. (2011) Trace and minor element variations and sulfur isotopes in crystalline and colloform ZnS: Incorporation mechanisms and implications for their genesis. Chemical Geology, 286, 118–134.

Reichert, J., and Borg, G. (2008) Numerical simulation and geochemical model of supergene carbonate-hosted nonsulphide zinc deposits. Ore Geology Reviews, 33,134–151

Reiser, F.K.M., Rosa, D.R.N., Pinto, Á.M.M., Carvalho, J.R.S., Matos, J.X., Guimarães, F.M.G., Alves, L.C., and de Oliveira, D.P.S. (2011) Mineralogy and geochemistry of tin- and germanium-bearing copper ore, Barrigão re-mobilized vein deposit, Iberian Pyrite Belt, Portugal. International Geology Review, 53, 1212–1238.

Saini-Eidukat, B., Melcher, F., Göttlicher, J., and Steininger, R. (2016) Chemical environment of unusually Ge- and Pb-rich willemite, Tres Marias Mine, Mexico. Minerals, 6, 20.

Santoro, L., Putzolu, F., Mondillo, N., Boni, M., and Herrington, R. (2020). Influence of Genetic Processes on Geochemistry of Fe-oxy-hydroxides in Supergene Zn Non-Sulfide Deposits. Minerals, 10(7), 602.

Si, R.J., Gu, X.X., Xie, L.X., and Zhang, N. (2013) Geological characteristics of the Fule polymetallic deposit in Yunnan province: a Pb-Zn deposit with dispersed elements and unusual enrichment. Geological Exploration, 49, 313–322 (in Chinese with English abstract).

Torró, L., Millán-Nuñez, A.J., Benites, D., González-Jiménez, J.M., Laurent, O., Tavazzani, L., Vallance, J., Chelle-Michou, C., Proenza, J.A., Flores, C., Melgarejo, J.C., Rosas, S., and Fontboté, L. (2023) Germanium- and gallium-rich sphalerite in Mississippi Valley–type deposits: the San Vicente district and the Shalipayco deposit, Peru. Mineralium Deposita, 58, 853–880

U.S. Geological Survey (2023) Mineral Commodity Summaries 2023. https://doi.org/10.3133/mcs2023

Vincent, V.I., Li, H., Girei, M.B., Förster, M.W., Ahmed, H.A., and Ntekim, E.E. (2021) In situ trace elements and sulfur isotope analysis of sulfides from the Akiri Cu±(Ag) deposit, Benue Trough, North-central Nigeria: Implications for ore genesis. Geochemistry, 81(4), 125801.

Wei, C., Huang, Z.L., Yan, Z.F., Hu, Y.S., and Ye, L. (2018) Trace element contents in sphalerite from the Nayongzhi Zn-Pb deposit, Northwestern Guizhou, China: Insights into incorporation mechanisms, metallogenic temperature and ore genesis. Minerals, 8(11), 490.

Wei, C., Ye, L., Hu, Y.S., Danyushevsky, L., Li, Z.L., and Huang, Z.L. (2019) Distribution and occurrence of Ge and related trace elements in sphalerite from the Lehong carbonate-hosted Zn-Pb deposit, northeastern Yunnan, China: Insights from SEM and LA-ICP-MS studies. Ore Geology Reviews, 115, 103175.

Wei, C., Ye, L., Hu, Y.S., Huang, Z.L., Danyushevsky, L., and Wang, H.Y. (2021) LA-ICP-MS analyses of trace elements in base metal sulfides from carbonate-hosted Zn-Pb deposits, South China: A case study of the Maoping deposit. Ore Geology Reviews, 130, 103945.

White, S.J.O., Piatak, N.M., McAleer, R.J., Hayes, S.M., Seal II, R.R., Schaider, L.A., and Shine, J.P. (2022). Germanium redistribution during weathering of Zn mine wastes: Implications for environmental mobility and recovery of a critical mineral. Applied Geochemistry, 143, 105341.

Xu, J., Cook, N.J., Ciobarnu, C.L., Li, X.F., Kontonikas-Charos, A., Gilbert, S., and Lv, Y.H. (2020) Indium distribution in sphalerite from sulfide–oxide–silicate skarn assemblages: a case study of the Dulong Zn–Sn–In deposit, Southwest China, Mineralium Deposita 56: 307–324

Ye, L., Cook, N.J., Ciobanu, C.L., Liu, Y.P., Zhang, Q., Liu, T.G., and Danyushevsky, L. (2011) Trace and minor elements in sphalerite from base metal deposits in South China: A LA-ICPMS study. Ore Geology Reviews, 39,188–217.

Ye, L., Li, Z.L., Hu, Y.S., Huang, Z.L., Zhou, Z.J., Fan, H.F., and Danyushevsky, L. (2016) Trace element in sulfide from Tianbaoshan Pb-Zn deposit, Sichuan province, China: A LA-ICPMS study. Acta Petrologica Sinica, 32(11), 3377–3393 (in Chinese with English abstract).

Zhang, Q.H. (1999). Geochemical studies on Dachang antimony ore deposit in Qinglong, Guizhou Province. Chinese Journal of Geochemistry 18(2):172–179.

Zhou, J.X., Luo, K., Wang, X.-C, Wilde, S.A., Huang, Z.L., Cui, Y.L., and Zhao, J.X. (2018) Ore genesis of the Fule Pb-Zn deposit and its relationship with the Emeishan Large Igneous Province: Evidence from mineralogy, bulk C-O-S and in situ S-Pb isotopes. Gondwana Research, 54, 161–179.

Zhu, D.P., Li, H., Tamehe, L.S., Jiang, W.C., Wang, C., and Wu, K.Y. (2022) Two-stage Cu–Pb–Zn mineralization of the Baoshan deposit in southern Hunan, South China: Constraints from zircon and pyrite geochronology and geochemistry. Journal of Geochemical Exploration, 241, 107070.

Zhu, C., Wen, H., Zhang, Y., Fu, S., Fan, H., and Cloquet, C. (2017). Cadmium isotope fractionation in the Fule Mississippi Valley-type deposit, Southwest China. Mineralium Deposita, 52, 675–686.

FIGURE CAPTION

FIGURE. 1 (**A**) Geological map of the Sichuan-Yunnan-Guizhou MVT province highlighting province boundary and the distribution of MVT Pb-Zn deposits. (**B)** Geological map of the Fule deposit and the A-B cross-section schematically revealing stratigraphy, structure, and orebodies (modified from Zhou et al. 2018). Yellow stars indicate sampling location, with numbers representing sample labels.

FIGURE. 2 Hand specimen and microscopic photographs. (**A**) Massive sulfide ores with brown-yellow sphalerite, galena and hydrothermal dolomite. (**B)** Brecciated sulfide ores containing pyrite-sphalerite-galena assemblage. **(C)** Banded sulfides-hydrothermal dolomite ore. **(D)** Weathered sulfide ores. (**E)** Massive willemite-dominated ores. (**F)** Vug-filled willemite and disseminated galena within the altered host rock. Mineral abbreviations: Py = pyrite; Sp = sphalerite; Gn = galena; HD = hydrothermal dolomite; Wil = willemite; Dol = dolostone.

FIGURE. 3 Reflected-light (A, D, F, H-L), back-scattered electron (B, G) and transmitted plane-polarized light photomicrographs (C, E) showing ore textures and mineral assemblages of the sulfide stage. (**A)** Pyrite 1 (Py1) is replaced by sphalerite 1a (Sp1a) containing abundant fine-grained chalcopyrite inclusions. (**B)** Tennantite replaces the Sp1a-Py1 assemblage. (**C)** Red-brown Sp1a overgrows with yellow-brown sphalerite (Sp1b). (**D)** Tennantite-galena (Gn1) vein crosscuts sphalerite (Sp1b) with discontinuous tails of chalcopyrite inclusions. (**E)** Red-brown Sp1a enclosed by yellow sphalerite (Sp2a) forming a zoned pattern. (**F)** Cavities-filling galena (Gn2) in the Sp2a matrix. (**G)** Galena 2 vein infills the fracture of inclusion-free Sp2a. (**H**) Coarse crystallized Sp2a replaced by Gn2. (**I)** Pyrite 2 (Py2) aggregates fills the vug/void of sphalerite 2b (Sp2b). (**J)** Calcite veins crosscut the Sp2b that overgrows with Py2 and Gn2. (**K)** Separate sphalerite 3 (Sp3) grains

enclosed by late formed galena 3 (Gn3). (**L**) Sphalerite (Sp3)-hydrothermal dolomite (HD2) replaced by Gn3. Mineral abbreviations: Py = pyrite; Sp = sphalerite; Gn = galena; Cpy = chalcopyrite; HD = hydrothermal dolomite; Ten = tennantite.

FIGURE. 4 Back-scattered electron (BSE) images highlight typical textural and minerals assemblages of supergene stage. (**A**) Willemite directly replaces original sphalerite; pre-existing cracks are filled with abundant fine-grained cerussite and greenockite. (**B**) Cerussite and smithsonite enclosed/replaced by willemite. (**C**) Willemite replaces irregularly shaped hematite grains. (**D**) Porous willemite replaces smithsonite, and the cavities are infilled with fine-grained hematite grains. (**E**) Cerussite aggregates are distributed in the margin of galena, which further is enclosed by willemite. (**F**) Aggregates of greenockite-cerussite enclose sphalerite and are further enveloped by willemite. Mineral abbreviations: Sp = sphalerite; Wil = willemite; Cer = cerussite; Smi = smithsonite; Gck = greenockite; Hem = hematite, Ap = apatite.

FIGURE. 5 Petrographic characteristics of five sphalerite types, highlighting each of these is different regarding textural relations, grain size, and mineral association. Mineral abbreviations: Py = pyrite; Sp = sphalerite; Gn = galena; Cpy = chalcopyrite; Ten = tennantite.

FIGURE. 6 Plots of the geometric mean concentrations for selected trace elements in five types of Fule sphalerite. (**A**) Mn. (**B**) Fe. (**C**) Cu. (**D**) Ge. (**E**) As. (**F**) Cd. (**G**) Ag. (**H**) Sb. Symbols represent the geomean, and the lower/upper error bars represent the lower/upper bound of the 95% confidence interval of the mean.

FIGURE. 7 Plots of the geometric mean concentrations for selected trace elements in Fule samples among different ore stages. (**A**) Ge. (**B**) Ni. (**C**) Tl. (**D**) Ag. (**E**) As. (**F**) Co. (**G**) Cd. (**H**) Sb. Symbols represent the geomean, and the lower/upper error bars represent the lower/upper bound of the 95%

confidence interval of the mean.

FIGURE. 8 LA-ICPMS element maps of the pyrite (Py1)-sphalerite (Sp1a)-tennantite (Ten)-galena assemblage (sample Fl14-65) from selected elements. Scales in counts-per-second (cps)

FIGURE. 9 LA-ICPMS element maps of an assemblage comprising sphalerite (Sp2a) and pyrite (Py2) for selected elements (sample FL-3). Scales in cps.

FIGURE. 10 LA-ICPMS element maps of an assemblage comprising sphalerite and willemite for selected elements (sample FL18-4). Scales in cps.

FIGURE. 11 LA-ICPMS element maps of an assemblage comprising smithsonite and willemite for selected elements (sample FL-15-2). Scales in cps.

FIGURE. 12 Binary correlation plots between Ge and Cu in different sphalerite types, with a trend sub-parallel to the (Ge/Cu) = 1/2 line.

FIGURE. 13 Binary diagrams showing mass ratios of minor/trace elements/Zn comparison between minerals. (**A)** sphalerite versus smithsonite. (**B)** sphalerite versus willemite.

Figure 1

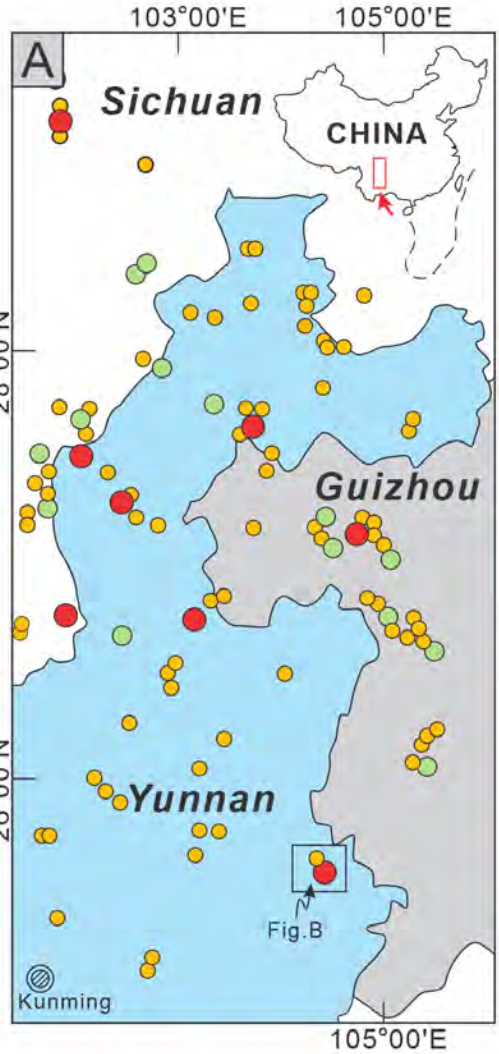

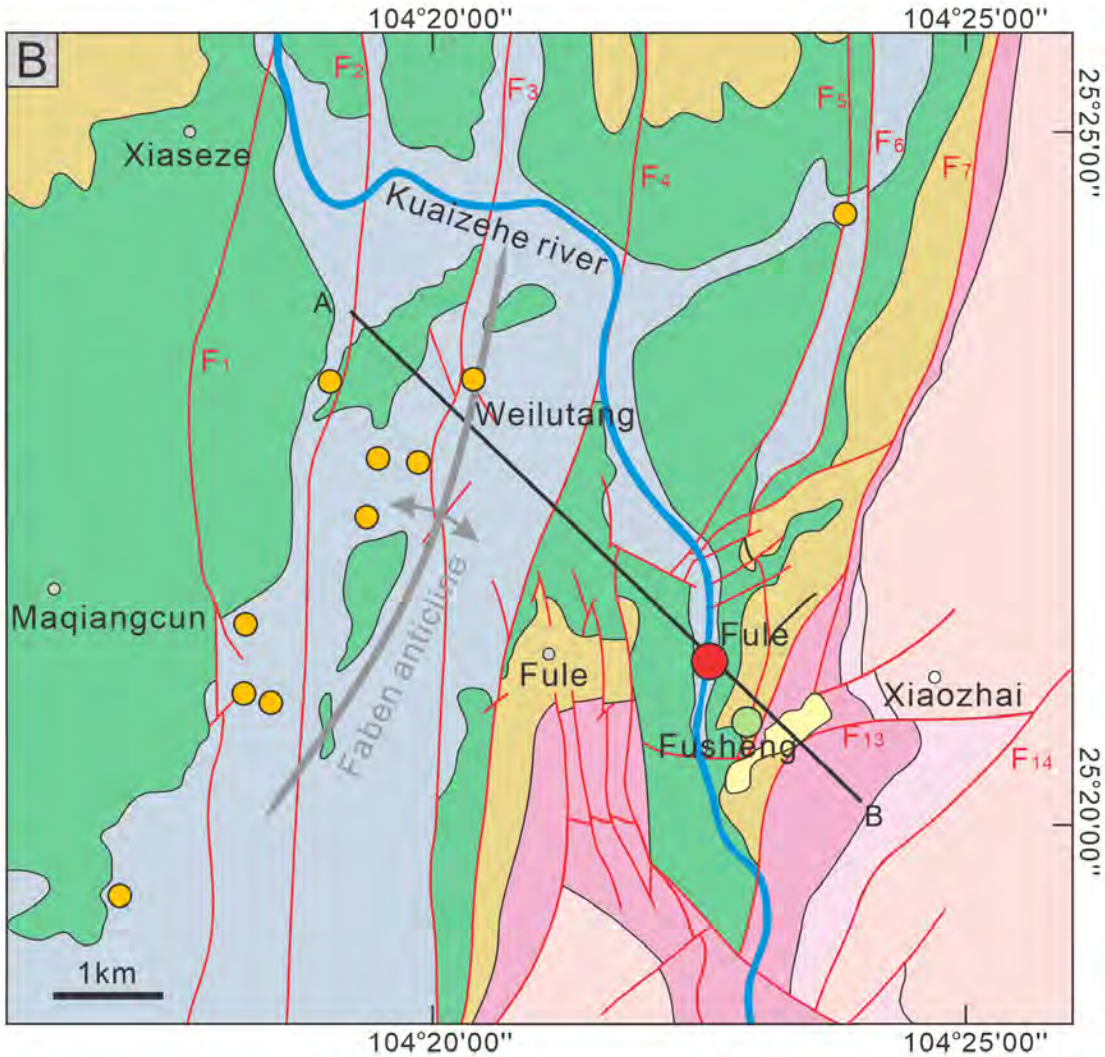

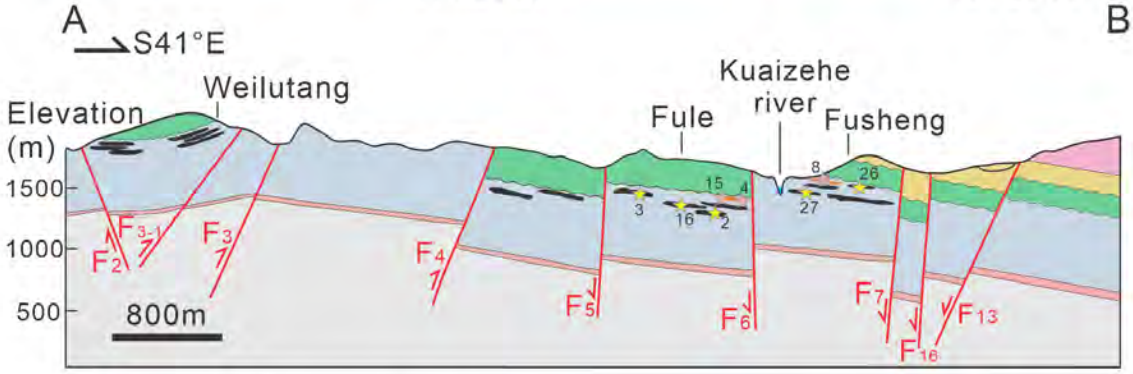

Figure A lengend

- Cities

Pb-Zn metal reserves

- >0.5 Mt deposits
- 0.2-0.5 Mt deposits
- <0.2 Mt deposits

Figure b lengend

- Quaternary
- Middle Triassic Guanling Fm.
- Early Triassic Yongning Fm.
- Early Triassic Feixianguan Fm.
- Late Permian Xuanwei Fm.
- Late Permian Emeishan basalts
- Middle Permian Yangxin Fm.
- Early Permian Liangshan Fm.
- Late Carboniferous Maping Fm.
- River
- Fault
- Sulfide-domiant orebody
- Oxide-domiant orebody
- Anticline
- Cross section line

Figure 2

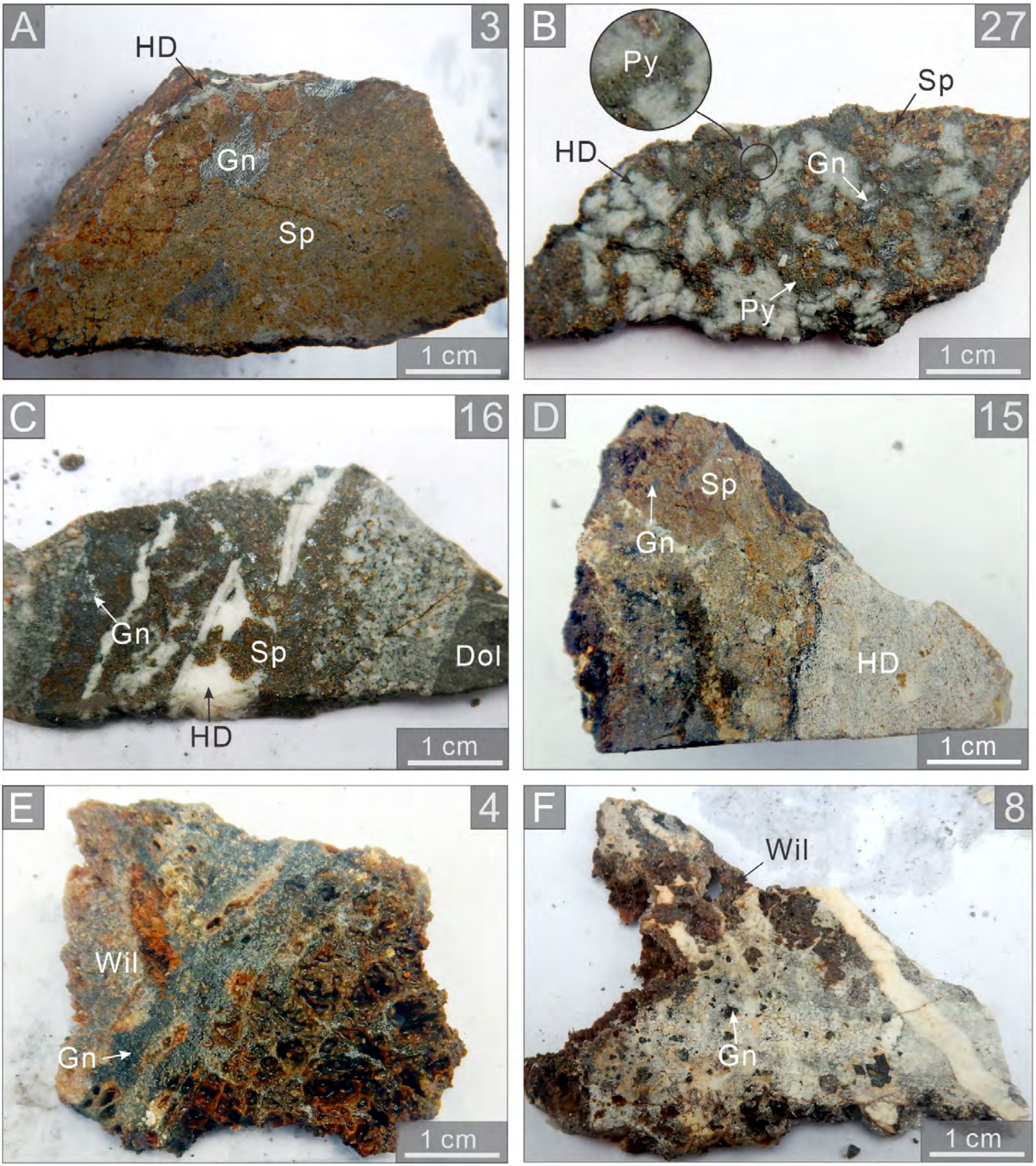
A
3
HD
Gn
Sp
1 cm
B
27
Py
Sp
HD
Gn
Py
1 cm
C
16
Gn
Sp
Dol
HD
1 cm
D
15
Sp
Gn
HD
1 cm
E
4
Wil
Gn
1 cm
F
8
Wil
Gn
1 cm

Figure 3

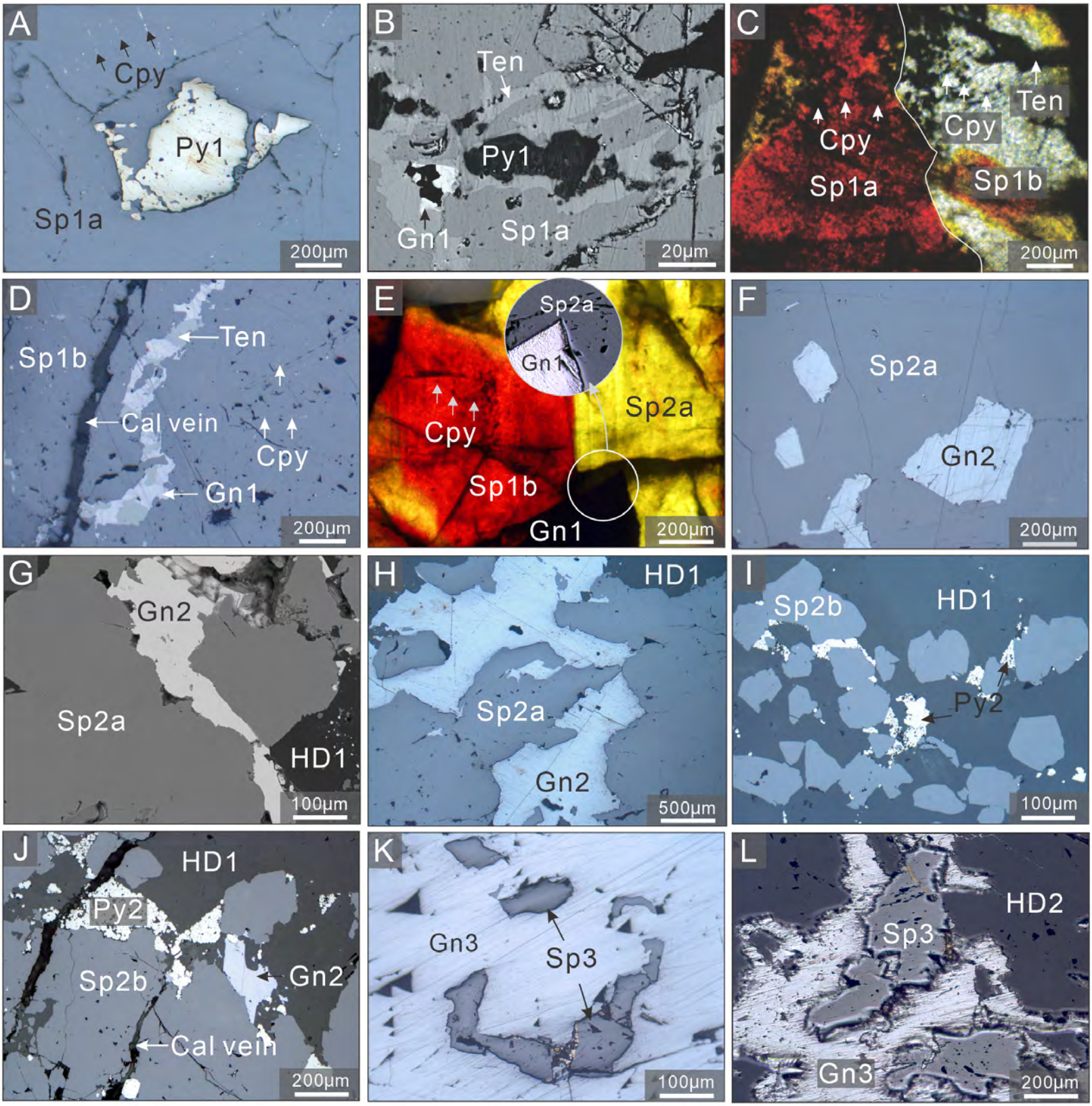
A
Cpy
Py1
Sp1a
200μm
B
Ten
Py1
Gn1
Sp1a
20μm
C
Cpy
Ten
Cpy
Sp1a
Sp1b
200μm
D
Sp1b
Ten
Cal vein
Cpy
Gn1
200μm
E
Sp2a
Gn1
Cpy
Sp2a
Sp1b
Gn1
200μm
F
Sp2a
Gn2
200μm
G
Gn2
Sp2a
HD1
100μm
H
HD1
Sp2a
Gn2
500μm
I
Sp2b
HD1
Py2
100μm
J
HD1
Py2
Sp2b
Gn2
Cal vein
200μm
K
Gn3
Sp3
100μm
L
HD2
Sp3
Gn3
200μm

Figure 4

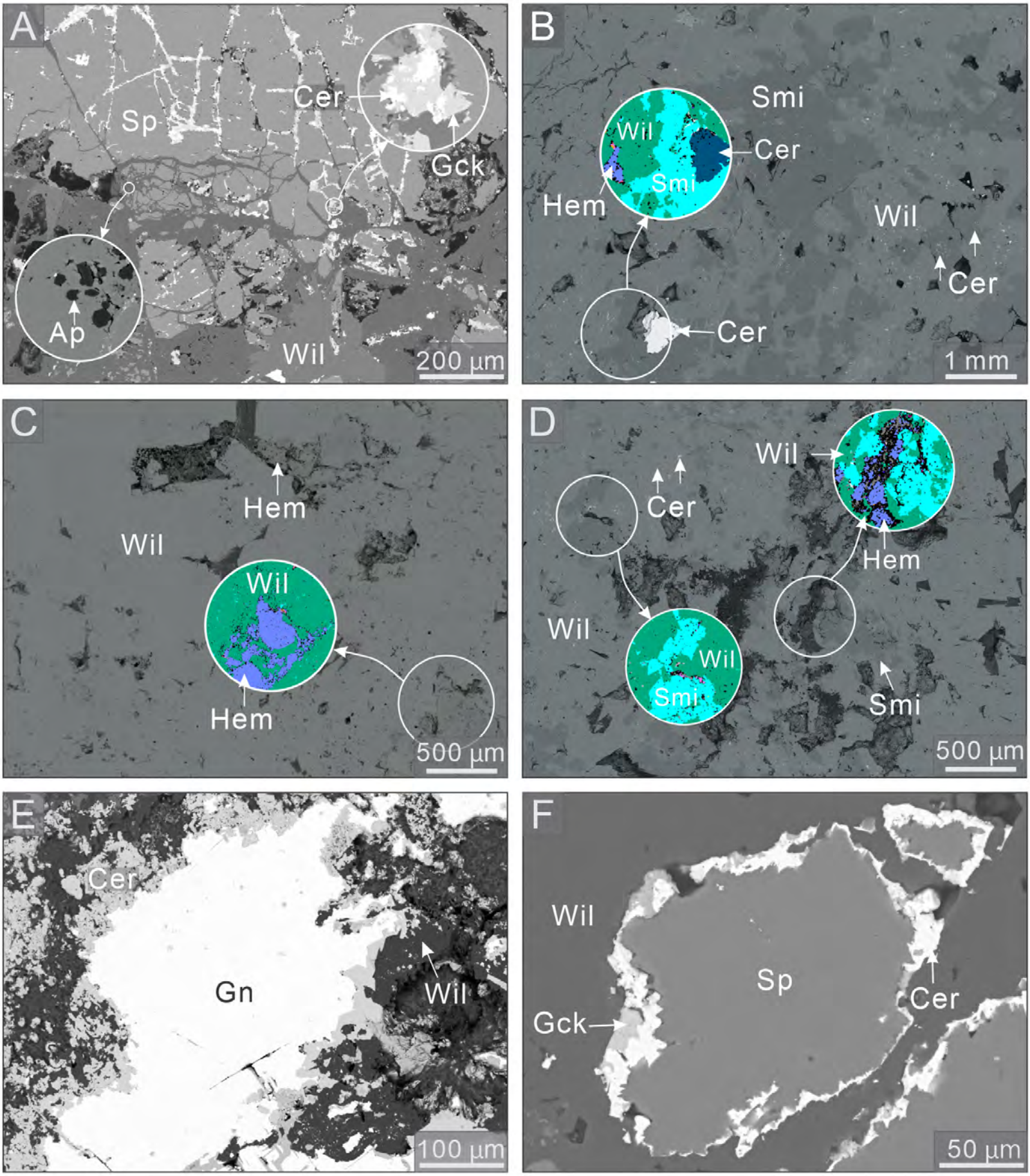
A
Cer
Sp
Gck
Ap
Wil
200 µm
B
Smi
Wil
Cer
Smi
Hem
Wil
Cer
Cer
1 mm
C
Hem
Wil
Wil
Hem
500 µm
D
Wil
Cer
Hem
Wil
Wil
Smi
Smi
500 µm
E
Cer
Gn
Wil
100 µm
F
Wil
Sp
Cer
Gck
50 µm

Figure 5

Sphalerite type	Textural relations and crystal shape		Examples
Sphalerite 1	**Contains abundant discontinuous trails of Cp inclusions**		
Sphalerite 1a	Encloses or replaces irregular shaped Py1 grains In some case, fine-grained Ten replaces Py1 and Sp1a martix		Fig. 3A-B
Sphalerite 1b	Red- to light-brown in color Crosscut by Ten-Gn1 veins or replaced by Ten		Fig.3C-D
Sphalerite 2	**Light-yellow color and free of mineral inclusions**		
Sphalerite 2a	Grain size >1 mm with irregular shaped Replaced or crosscut by Gn2		Fig.3F-H
Sphalerite 2b	Grain size <500 um Overgrow or is crosscut by fine-grained Py2 aggregates		Fig.3I-J
Sphalerite 3	**Separate grains or inclusions in the Gn3 matrix**		
Sphalerite 3	Grain: quadrangular and elliptic oval shapes enclosed by Gn3 grains, accom panied with minor Py2		Fig.3K-L

Figure 6

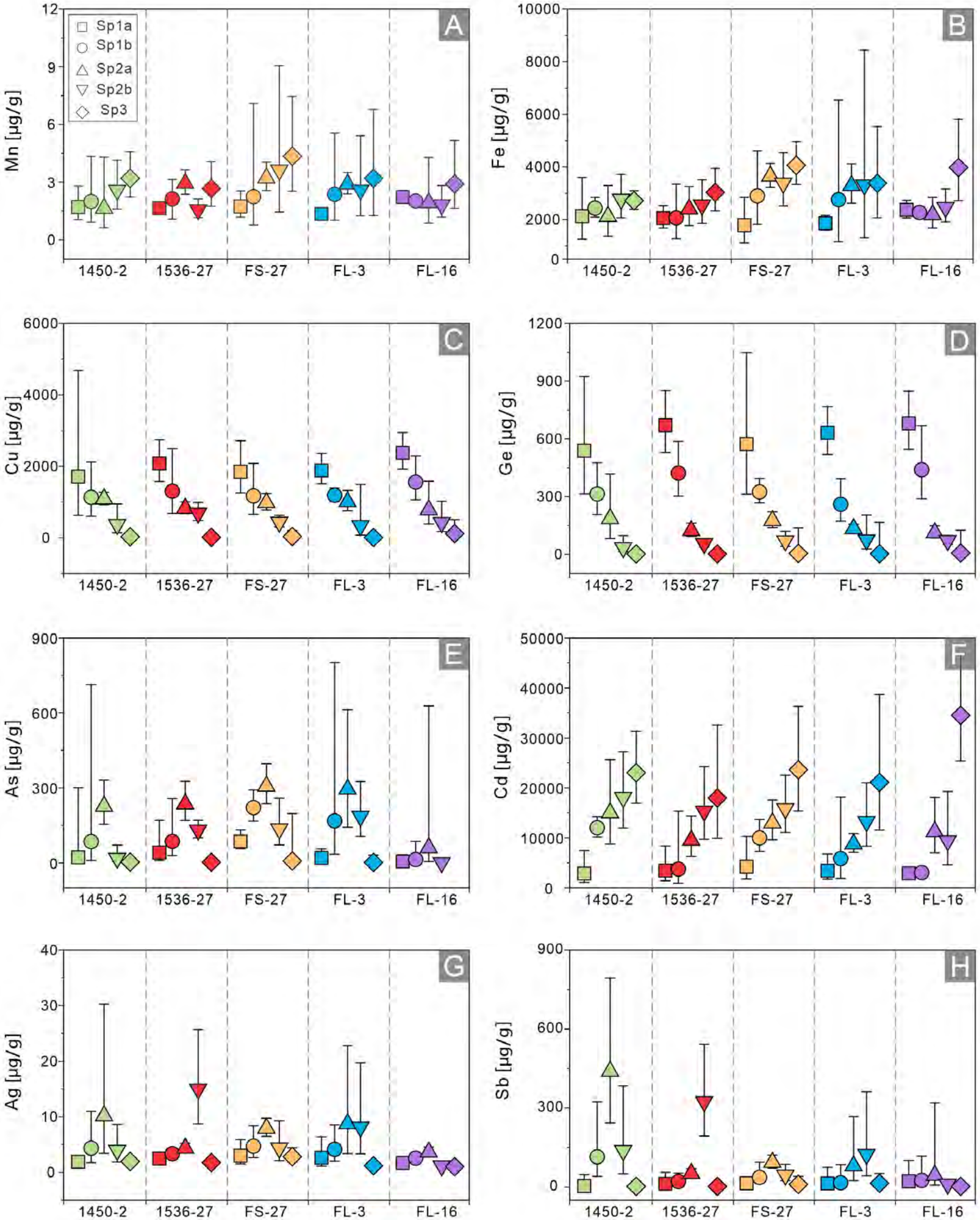
A
B
C
D
E
F
G
H
Sp1a
Sp1b
Sp2a
Sp2b
Sp3
Mn [µg/g]
Fe [µg/g]
Cu [µg/g]
Ge [µg/g]
As [µg/g]
Cd [µg/g]
Ag [µg/g]
Sb [µg/g]
1450-2
1536-27
FS-27
FL-3
FL-16

Figure 7

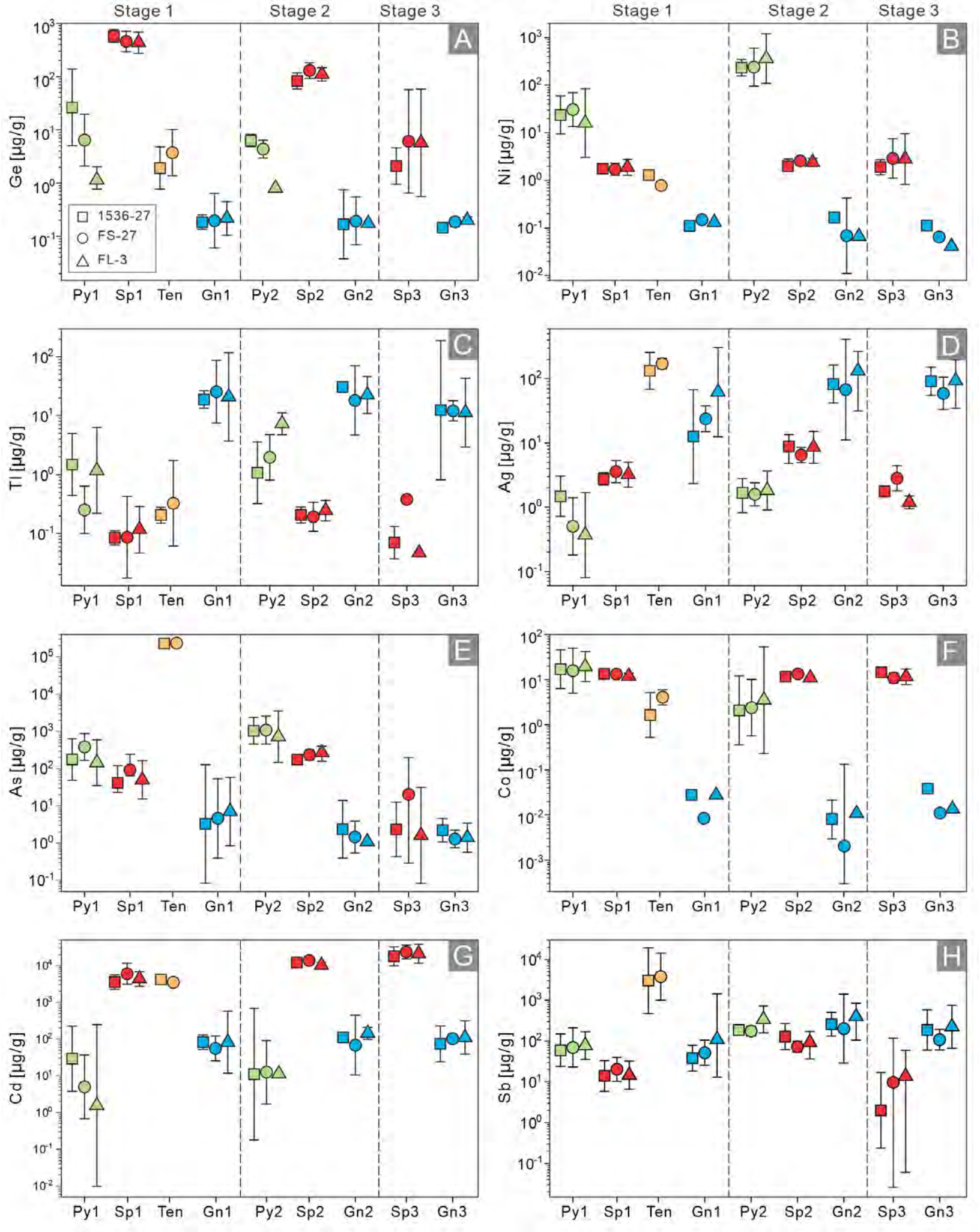
Stage 1
Stage 2
Stage 3
A
B
C
D
E
F
G
H
Ge [µg/g]
Ni [µg/g]
Tl [µg/g]
Ag [µg/g]
As [µg/g]
Co [µg/g]
Cd [µg/g]
Sb [µg/g]
1536-27
FS-27
FL-3
Py1
Sp1
Ten
Gn1
Py2
Sp2
Gn2
Sp3
Gn3

Figure 8

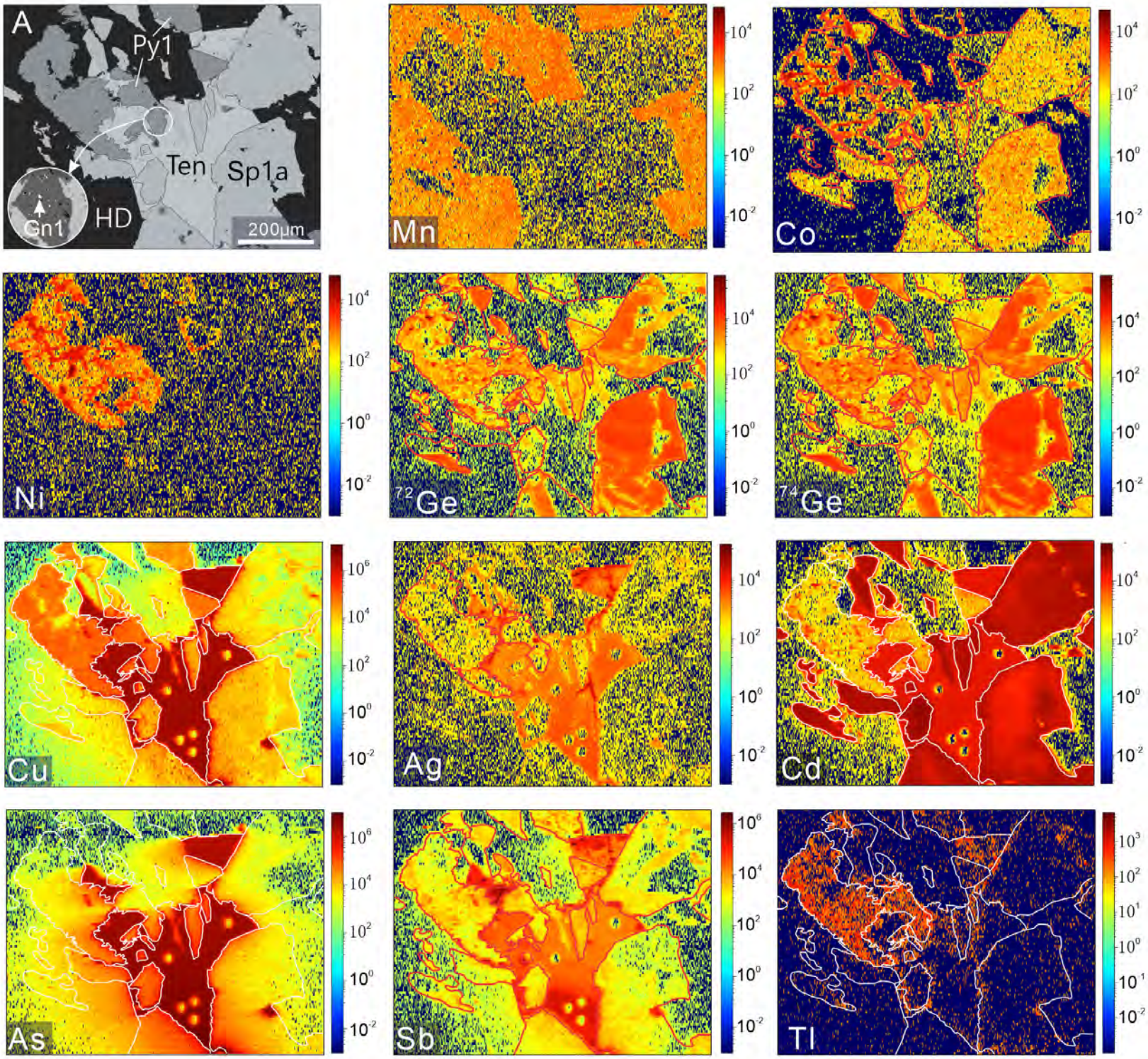

Figure 9

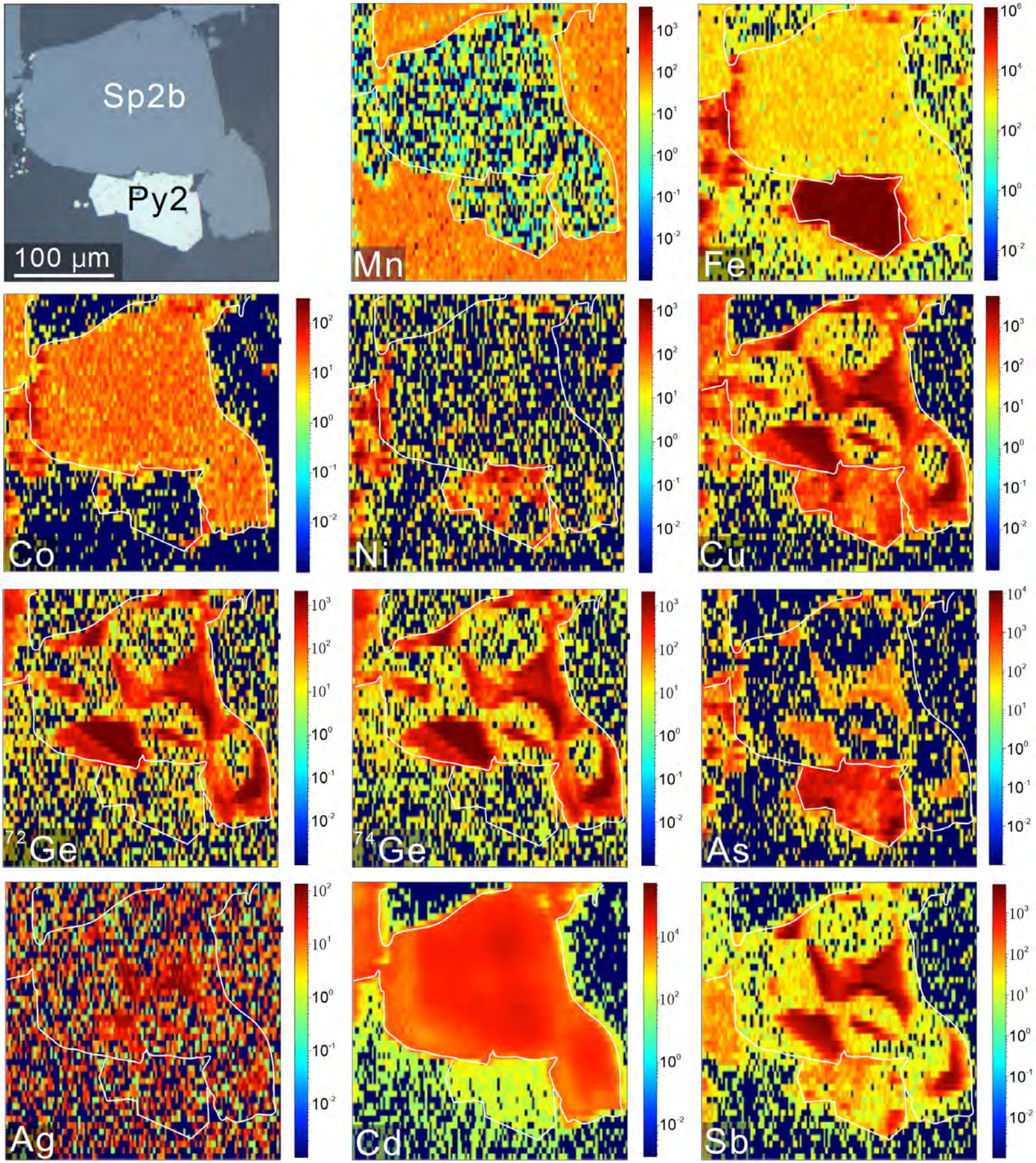

Figure 10

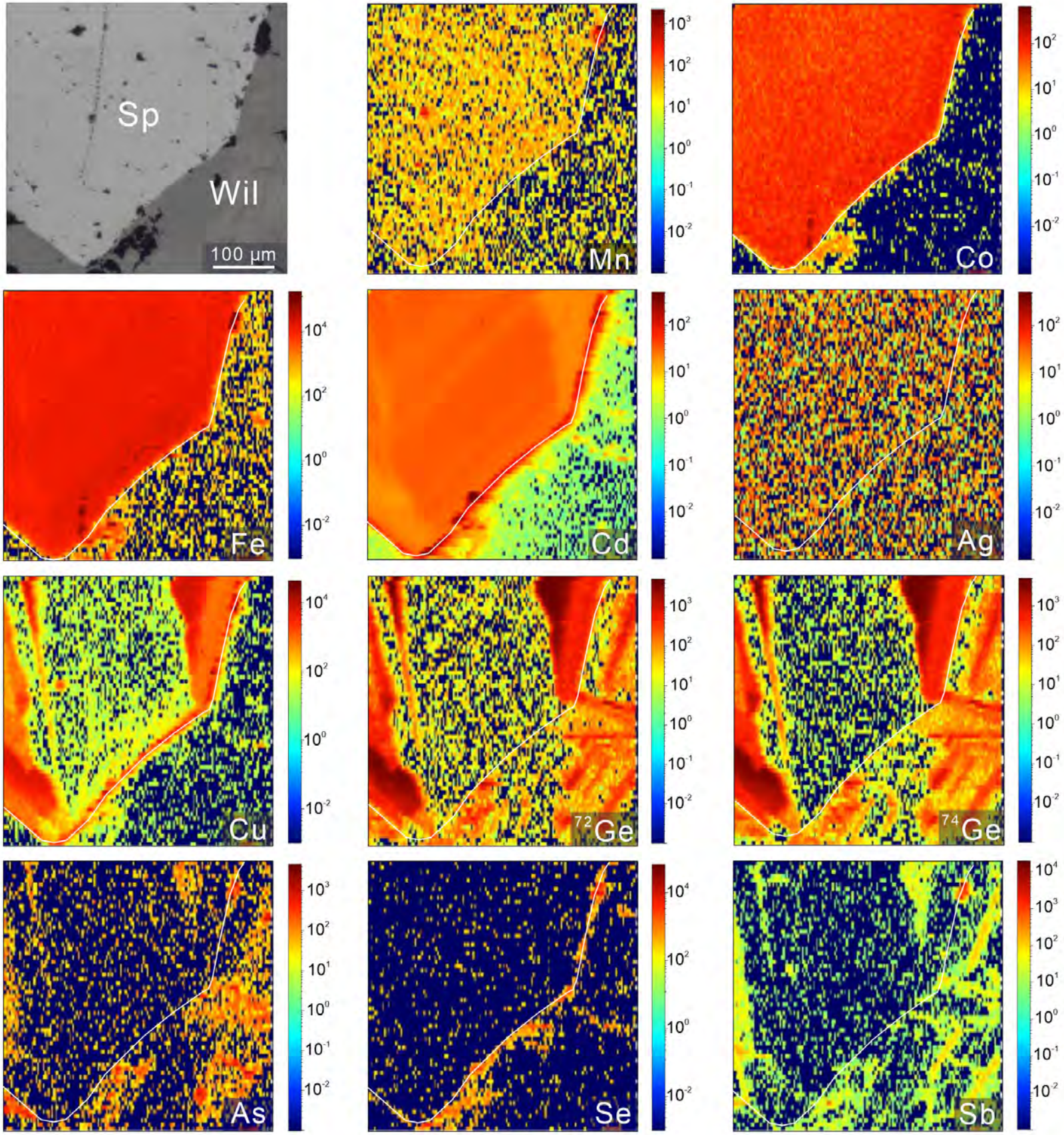

Figure 11

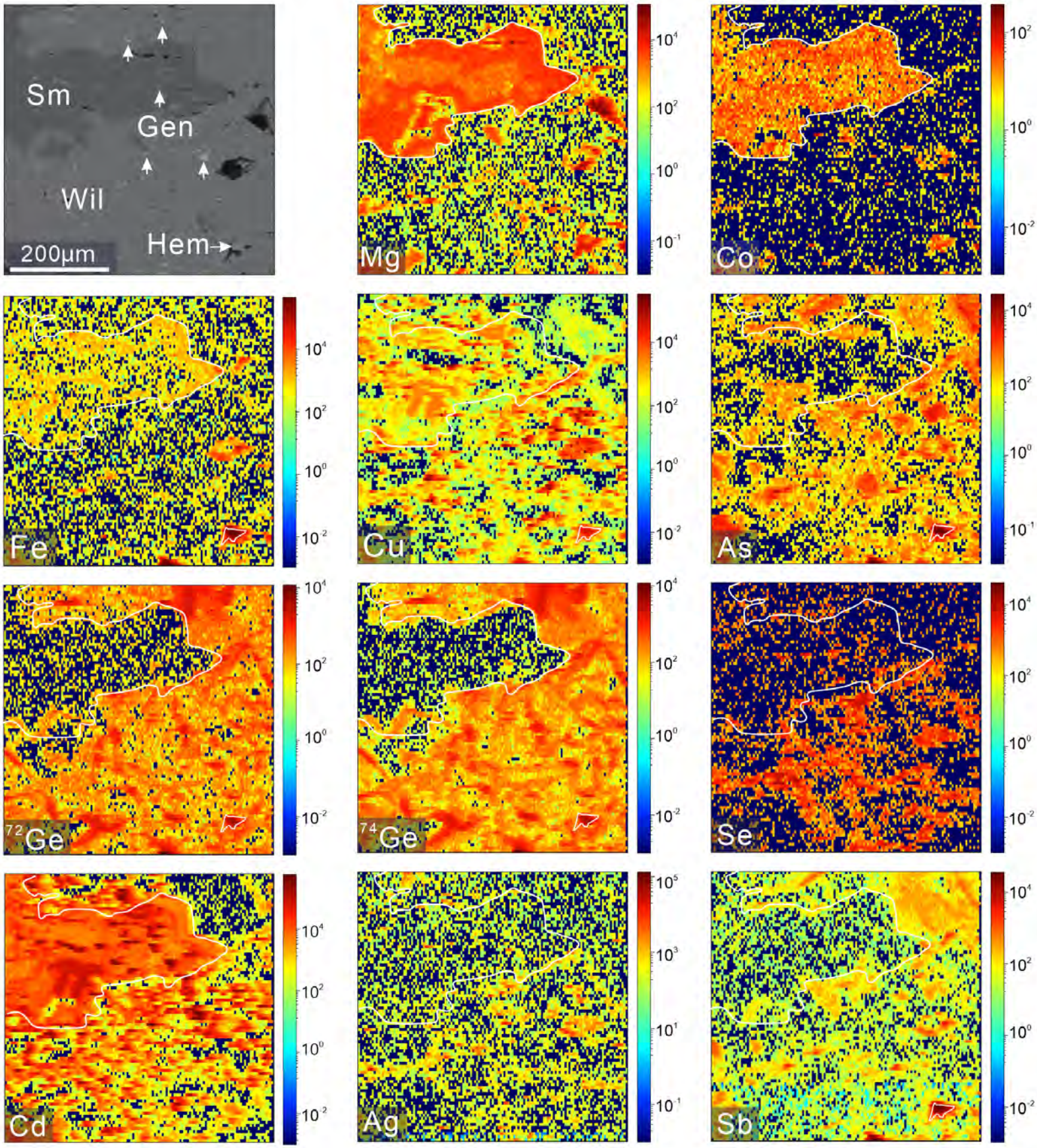

Figure 12

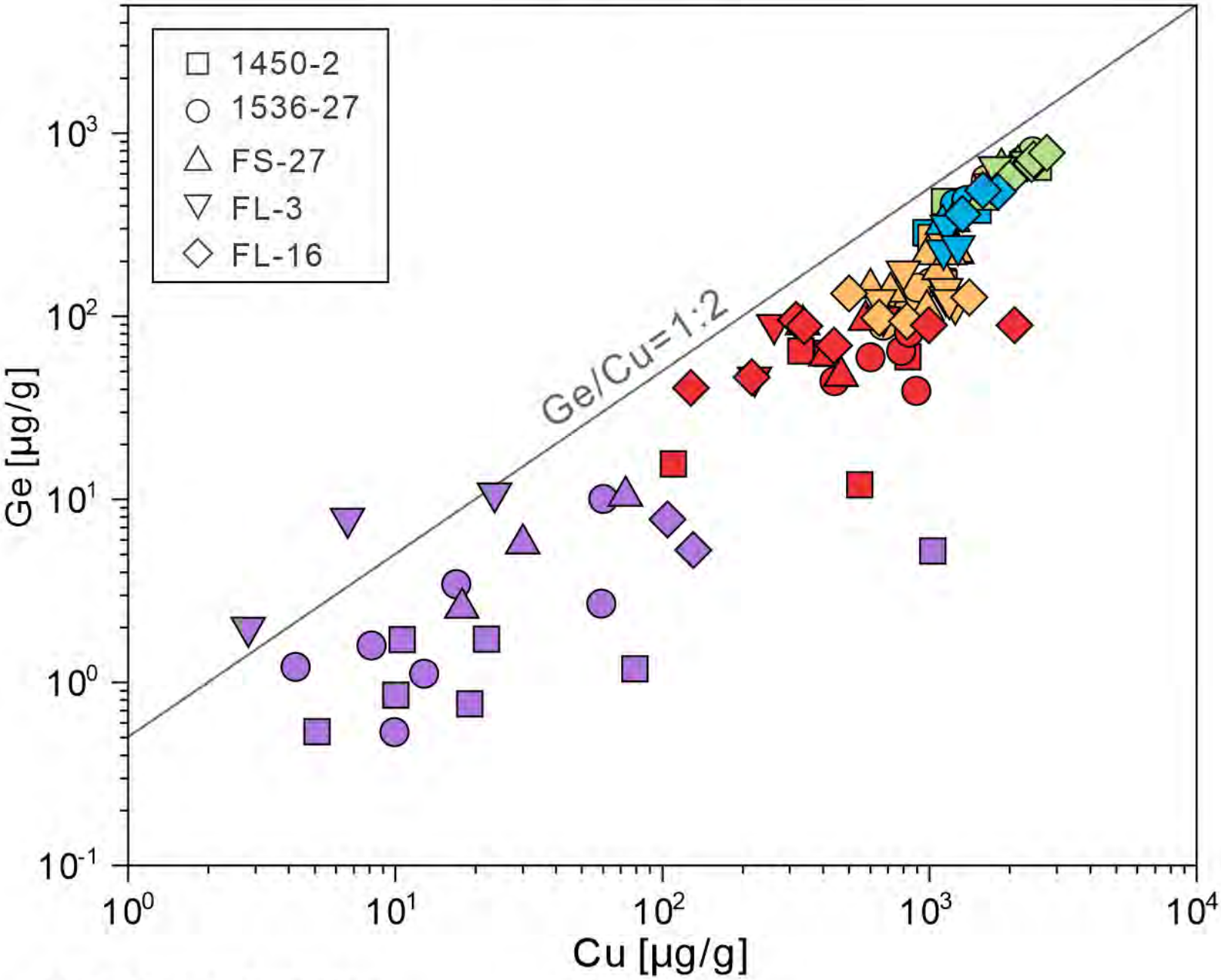

Sphalerite textures

- Sp1a Sphalerite with chalcopyrite is enclosed by irregular shaped pyrite
- Sp1b Sphalerite with chalcopyrite is crosscut by galena and tennantite
- Sp2a Coarse-grain sphalerite is replaced by galena
- Sp2b Fine- to coarse-grain sphalerite overgrows with pyrite aggregates
- Sp3 Fine-grain sphalerite is enclosed by galena

Figure 13

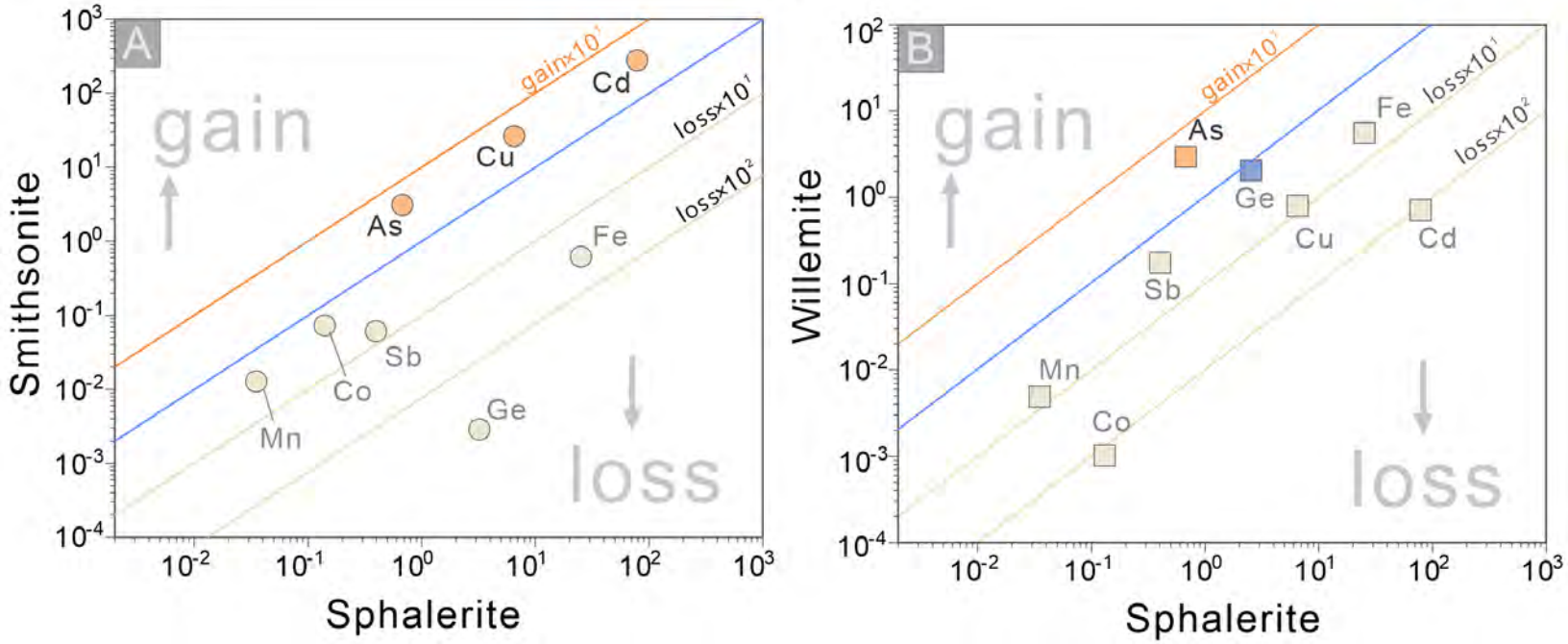
A
gain
loss
gainx10¹
lossx10¹
lossx10²
Cd
Cu
As
Fe
Sb
Co
Mn
Ge
Smithsonite
Sphalerite
B
gain
loss
gainx10¹
lossx10¹
lossx10²
As
Fe
Ge
Cu
Cd
Sb
Mn
Co
Willemite
Sphalerite